Journal of Computational Physics 510 (2024) 113072

Contents lists available at ScienceDirect

Journal of Computational Physics

journal homepage: www.elsevier.com/locate/jcp

Essentially non-hourglass SPH elastic dynamics

Shuaihao Zhang [a,b], Sérgio D.N. Lourenço [a], Dong Wu [b], Chi Zhang [b,c], Xiangyu Hu [b,*]

[a] Department of Civil Engineering, The University of Hong Kong, Pokfulam, Hong Kong Special Administrative Region of China
[b] School of Engineering and Design, Technical University of Munich, 85748 Garching, Germany
[c] Huawei Technologies Munich Research Center, 80992 Munich, Germany

ARTICLE INFO

Keywords:
Smoothed particle hydrodynamics
Hourglass modes
Numerical instability
Updated Lagrangian formulation
Elastic dynamics

ABSTRACT

More than two decades ago, the numerical instabilities of particle clustering and non-physical fractures encountered in the simulations of typical elastic dynamics problems using updated Lagrangian smoothed particle hydrodynamics (ULSPH) was identified as tensile instability. Despite continuous efforts in the past, a satisfactory resolution for the simulations of these problems has remained elusive. In this paper, the concept of hourglass modes, other than tensile instability, is first explored for the discretization of shear force, arguing that the former may actually lead to the numerical instabilities in these simulations. Based on such concept, we present an essentially non-hourglass formulation by utilizing the Laplacian operator which is widely used in fluid simulations. Together with the dual-criteria time stepping, adopted into the simulation of solids for the first time to significantly enhance computational efficiency, a comprehensive set of challenging benchmark cases is used to showcase that our method achieves accurate and stable SPH elastic dynamics.

1. Introduction

Smoothed particle hydrodynamics (SPH), original proposed by Lucy [1] and Gingold and Monaghan [2] for simulating astrophysical problems, is a fully Lagrangian particle-based method. In SPH, the physical quantities such velocity, position, and stress are carried by each particle, and the motion of particles is described in the Lagrangian framework, which is naturally well-suited for simulating problems involving large deformations, especially fracture and failure. Over the past 40 years, SPH has been extensively developed and improved, and it has been successfully applied to simulate various physical problems including fluid dynamics [3–6], solid dynamics [7–11], and fluid-solid interactions [12–15].

Based on whether the particle configurations, which define the neighbors of each particle, are updated during the simulation, the SPH methods for solid dynamics can be classified into the total Lagrangian SPH (TLSPH) [16] and updated Lagrangian SPH (ULSPH) [7,17]. TLSPH and ULSPH cater to different domains and address specific sets of physical problems based on their unique characteristics. TLSPH is able to handle the elastic and plastic dynamics efficiently as it saves the time required for updating particle configurations. Compared with TLSPH, while ULSPH is able to cope with material failure and fracture beyond elastic or plastic deformations more naturally with updating particle configurations at each time step, it faces two important drawbacks associated with elastic dynamics: one is the persistent issue of the numerical instability (particle clustering and numerical fractures); the other is poorer efficiency due to the computational effort and memory latency when the particle configurations are updated frequently.

* Corresponding author.
E-mail address: xiangyu.hu@tum.de (X. Hu).

https://doi.org/10.1016/j.jcp.2024.113072
Received 29 August 2023; Received in revised form 23 April 2024; Accepted 30 April 2024

Available online 7 May 2024

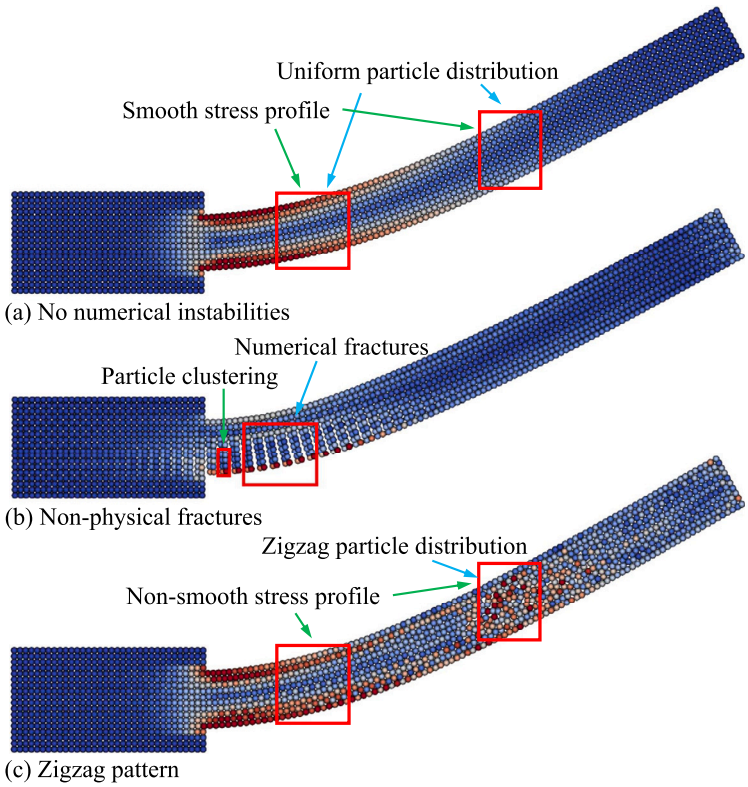

Fig. 1. Illustration for (a) no numerical instabilities, (b) non-physical fractures and (c) zigzag pattern in ULSPH simulations of 2D oscillating plates. The particles are colored with von Mises stress.

As shown in Fig. 1b for a typical example, the numerical instability involving particle clustering and non-physical fractures presented in the simulations of many elastic dynamics problems with the standard ULSPH formulation is often considered as tensile instability, a fundamental numerical issue caused by the tensile stress and was introduced by Swegle et al. [18] in 1995. Since then, different approaches have been proposed to address this problem [19–23]. However, these methods also have their own issues, such as failure to maintain conservation properties, low computational efficiency, or limited applicability, being only suitable for specific cases rather than universally applicable [24–26]. Later, in 2000, inspired by the repulsive interactions observed among closely spaced atoms, Monaghan [17] introduced a small repulsive force (named the artificial stress) between particles in SPH based on the concept of counteracting the tension to prevent particle clustering and then remove the instability. Gray et al. [7] further developed this approach by determining the parameters in artificial stress from the dispersion relation for elastic waves. Despite the broader recognition compared to many other approaches in addressing the instability in SPH elastic dynamics, the artificial stress method still faces the following limitations: (1) it has two parameters requiring case-dependent tuning; (2) it may fail in scenarios where the deformation is significant or when dealing with materials featuring high Poisson's ratio [27,28]; (3) its extension for three-dimensional (3D) simulations is yet to be developed. The third issue is due to the fact that the derivation of the artificial stress term is based on a two-dimensional (2D) scenario [7], and this approach is not only computationally intensive but also difficult to perform in 3D scenarios [29,30]. To our best knowledge, there are no documented instances utilizing this artificial stress term directly in 3D simulations.

An interest phenomenon one can observe is that, as shown in Fig. 1c, although the artificial stress can eliminate non-physical fractures in some cases, the artifacts with zigzag patterns appear in the stress profile. This issue is not unique for the specific cases, and can be found in other ULSPH methods aimed at mitigating tensile instability [27,31]. The zigzag pattern is a typical numerical instability phenomenon well known as hourglass modes, another fundamental numerical issue related to collocation methods [32,33]. Hourglass modes were also found in TLSPH elastic dynamics, when the deformation is very large [32], even though TLSPH does not suffer from the tensile instability [16].

In this work, based on the above observations, we propose to address the numerical instability observed in the ULSPH simulations of elastic dynamics problems, i.e., non-physical fractures and zigzag patterns, in the respect of hourglass modes other than tensile instability. From this very different point of view, we develop a non-nested ULSPH formulation for computing the shear stress induced acceleration and essentially eliminate the hourglass modes. With extensive numerical examples, we show that the new formulation is numerically stable and able to obtain very smooth particle distribution and stress profiles (as shown in Fig. 1a for a typical example.) Note that, different from reference [7], the present formulation works for both 2D and 3D scenarios. Also note that, unlike the

tensile-instability control (TIC) method [31] requiring to identify inner and surface particles for different treatments, the present method doses not lead to such complexity.

Another contribution of this work is that, to improve computational efficiency, a dual-criteria time stepping method [34] is incorporated into ULSPH simulations of elastic dynamics for the first time. There are two time steps named the advection time step and the much smaller acoustic time step. By updating of particle configurations only in the advection time step, the frequency for updating particle configurations can be minimized, and the calculation time can be reduced. It is worth mentioning that the speed of sound in solid simulations is the true sound speed, much higher than the artificial sound speed used in the weekly compressible SPH (WCSPH) method for fluids. This implies the dual-criteria time stepping scheme leads to a significant enhancement in computational efficiency for solid simulations.

The remainder of this article is arranged as follows. The basic theory of elastic dynamics is introduced in Section 2. The original formulation and the present essentially non-hourglass formulation for elastic dynamics are described in Section 3 and Section 4 respectively. The dual-criteria time stepping scheme for solid simulations is described in Section 5, and a set of benchmark cases for elastic dynamics are then used to validate the convergence, accuracy and stability of the proposed method in Section 6. Section 7 draws the conclusion. For future in-depth research, all the code used in this study has been open-sourced in the SPHinXsys repository [35] at https://www.sphinxsys.org and https://github.com/Xiangyu-Hu/SPHinXsys.

2. Governing equations and constitutive relations

In a Lagrangian framework, the governing equations include mass and momentum conservation for continuum mechanics are defined as

$$\frac{\mathrm{d}\rho}{\mathrm{d}t} = -\rho\nabla\cdot\mathbf{v} \tag{1}$$

$$\frac{\mathrm{d}\mathbf{v}}{\mathrm{d}t} = \frac{1}{\rho}\nabla\cdot\boldsymbol{\sigma} + \mathbf{g} \tag{2}$$

where ρ is the density, $\mathbf{v}$ is velocity, t is the time, $\boldsymbol{\sigma}$ is the stress tensor, and $\mathbf{g}$ is the body force. The total stress tensor $\boldsymbol{\sigma}$ can be divided into two terms, i.e., the hydrostatic pressure and the shear stress, as shown below.

$$\boldsymbol{\sigma} = -p\mathbf{I} + \boldsymbol{\sigma}^s \tag{3}$$

where p is the hydrostatic pressure, $\mathbf{I}$ is the identity matrix, and $\boldsymbol{\sigma}^s$ is the shear stress. The pressure p can be evaluated from density based on an artificial equation of state [7].

$$p = c_0^2(\rho - \rho_0) \tag{4}$$

where ρ_0 and ρ are the initial and the current density respectively. c_0 is the sound speed, which is expressed as [27]

$$c_0 = \sqrt{\frac{E}{3(1-2\nu)\rho_0}} \tag{5}$$

where E is the Young's modulus, ν is the Poisson's ratio of the given material. The shear stress is the integral of the shear stress rate with respect to time.

$$\boldsymbol{\sigma}^s = \int_0^t \dot{\boldsymbol{\sigma}}^s \mathrm{d}t \tag{6}$$

For a linear elastic model, the shear stress rate is defined as

$$\dot{\boldsymbol{\sigma}}^s = 2G(\dot{\boldsymbol{\epsilon}} - \frac{1}{d}tr(\dot{\boldsymbol{\epsilon}})\mathbf{I}) \tag{7}$$

where G is the shear modulus. $tr(\varphi)$ indicates the trace of a variable φ and $\dot{\varphi}$ is the change rate with time for the variable φ (φ is an arbitrary variable). d represents the space dimension, and $d = 2$ and 3 for 2D and 3D cases respectively. $\dot{\boldsymbol{\epsilon}}$ is strain rate, which is defined as

$$\dot{\boldsymbol{\epsilon}} = \frac{1}{2}(\nabla\mathbf{v} + (\nabla\mathbf{v})^T) \tag{8}$$

where $\nabla\mathbf{v}$ donates the velocity gradient, and superscript T indicates the transpose of a tensor.

3. Original SPH formulation

According to Eq. (2) and Eq. (3), The acceleration related to volumetric (hydrostatic pressure) and deviatoric part (shear stress) of the stress tensor can be express as

$$\dot{\mathbf{v}}^p = -\frac{1}{\rho}\nabla p \tag{9}$$

$$\dot{\mathbf{v}}^s = \frac{1}{\rho}\nabla \cdot \boldsymbol{\sigma}^s \tag{10}$$

where $\dot{\mathbf{v}}^p$ and $\dot{\mathbf{v}}^s$ donate the velocity change rate (acceleration) induced by hydrostatic pressure and shear stress respectively. Then the total velocity change rate $\dot{\mathbf{v}} = \dot{\mathbf{v}}^p + \dot{\mathbf{v}}^s + \mathbf{g}$.

A low-dissipation Riemann solver [36,37] is incorporated in the WCSPH to discrete the continuity equation and the momentum equation for hydrostatic pressure.

$$\frac{\mathrm{d}\rho_i}{\mathrm{d}t} = 2\rho_i \sum_j \frac{m_j}{\rho_j}(U^* - \mathbf{v}_{ij}\mathbf{e}_{ij})\frac{\partial W_{ij}}{\partial r_{ij}} \tag{11}$$

$$\frac{\mathrm{d}\mathbf{v}_i^p}{\mathrm{d}t} = -2\sum_j m_j \frac{P^*}{\rho_i \rho_j}\nabla_i W_{ij} \tag{12}$$

Here, W_{ij} represents $W(\mathbf{r}_i - \mathbf{r}_j, h)$, which is the kernel function. $\mathbf{r}$ is particle position and h is the smoothing length. The subscripts i and j donate particle numbers, and m is the particle mass. $\mathbf{e}_{ij}$ is the unit vector pointing from particle j to particle i and $\mathbf{v}_{ij} = \mathbf{v}_i - \mathbf{v}_j$. $\nabla_i W_{ij} = \frac{\partial W(r_{ij},h)}{\partial r_{ij}}\mathbf{e}_{ij}$ is the derivative of kernel function, and $r_{ij} = |\mathbf{r}_i - \mathbf{r}_j|$ is the distance between two particles. U^* and P^*, which are obtained from the low-dissipation Riemann solver [36,37], are the solutions of an inter-particle Riemann problem along the unit vector pointing from particle i to j. U^* and P^* are expressed as [36]

$$U^* = \frac{\rho_L c_L U_L + \rho_R c_R U_R + P_L - P_R}{\rho_L c_L + \rho_R c_R} \tag{13}$$

$$P^* = \frac{\rho_L c_L P_R + \rho_R c_R P_L + \beta \rho_L c_L \rho_R c_R (U_L - U_R)}{\rho_L c_L + \rho_R c_R} \tag{14}$$

The subscripts L and R indicate the left and right states from Riemann problem, and are defined as

$$\begin{cases} (\rho_L, U_L, P_L, c_L) = (\rho_i, \mathbf{v}_i \cdot \mathbf{e}_{ij}, P_i, c_{0i}) \\ (\rho_R, U_R, P_R, c_R) = (\rho_j, \mathbf{v}_j \cdot \mathbf{e}_{ij}, P_j, c_{0j}) \end{cases} \tag{15}$$

c_0 is the speed of sound as defined in Eq. (5). β in Eq. (14) is a dissipation limiter, which is set as [36]

$$\beta = \min\{3\max\left[\frac{(P_L + P_R)(U_L - U_R)}{\rho_L c_L + \rho_R c_R}, 0\right], 1.0\} \tag{16}$$

The shear acceleration $\dot{\mathbf{v}}^s$ can be discretized by

$$\frac{\mathrm{d}\mathbf{v}_i^s}{\mathrm{d}t} = \sum_j m_j \frac{\boldsymbol{\sigma}_i^s + \boldsymbol{\sigma}_j^s}{\rho_i \rho_j} \cdot \nabla_i W_{ij} \tag{17}$$

Refer to Eq. (6)-Eq. (8), the velocity gradient needs to be discretized for computing shear stress $\boldsymbol{\sigma}_i^s$ and $\boldsymbol{\sigma}_j^s$, which has the following form [38]

$$\nabla \mathbf{v} = \sum_j \mathbf{v}_{ij} \otimes \nabla_i W_{ij} V_j \tag{18}$$

where V_j is the volume of particle j.

In the original SPH formulation, it is evident that shear acceleration $\dot{\mathbf{v}}^s$ is derived from the shear stress by Eq. (17). To compute the shear stress, the process involves initially determining velocity gradients by Eq. (18), followed by calculating strain rates with Eq. (8). Subsequently, the stress rate is evaluated by Eq. (7), and integrating the stress rate over time based on Eq. (6) yields the shear stress. In the entire process, it is observed that two consecutive summations are performed on neighboring particles. Additionally, the result of the first summation (Eq. (18)) serves as an input variable in the second summation (Eq. (17)), revealing a nested structure, referred to by Morris et al. [3] as "nested summation" and by Hu and Adams [6,39] later as "nested application".

4. Essentially non-hourglass SPH formulation

The formulation in section 3 suffers from hourglass issues induced by zero energy modes [40], which is characterized by a pattern of particle displacement that does not correspond to rigid body motion but still results in zero strain energy [40–42]. As shown in Fig. 2, we use a simple case to demonstrate the zero energy modes. The particles are uniformly distributed along the x-axis, and the particles change from time step n to time step $n+1$ with the velocity $v_i = v_1 = v_4 = -v_2 = -v_3$. Under these circumstances, the original SPH calculations yield a zero velocity gradient for particle i based on Eq. (18), consequently leading to a negligible stress increment. In other words, this deformation mode is not resisted [41] and, naturally, cannot recover even under elastic deformation conditions, which leads to an inaccurate estimation of the shear stress and shear acceleration [33].

In a recent effective remedy for hourglass modes in TLSPH [33], the particle acceleration due to the divergence of shear stress is directly obtained from a one-step Laplacian formulation of the particle displacement other than the nested implementation of the 2nd-order derivatives used in the original TLSPH. Actually, such non-nested SPH formulation of Laplacian is widely used in SPH

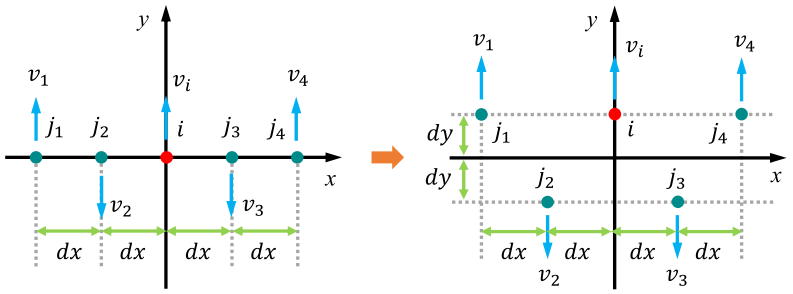

Fig. 2. Illustration of zero energy modes by considering a simple case. The particles are uniformly distributed along the x-axis, and change from time step n to time step $n+1$ with the velocity perpendicular to the x-axis ($v_i = v_1 = v_4 = -v_2 = -v_3$).

fluid dynamics for computing the viscous-force term in the Navier-Stokes equations [3,6,43], and is found much stabler than the nested counterpart. Inspired by these previous solutions, we apply a Laplacian operator to calculate the shear acceleration directly in ULSPH simulations of elastic dynamics.

Firstly, we re-formulated the theoretical expression for shear acceleration by combining Eq. (6)-Eq. (10)

$$\dot{\mathbf{v}}^s = \frac{G}{\rho}\nabla \cdot \int_0^t (\nabla \mathbf{v} + (\nabla \mathbf{v})^T - \frac{2}{d}\nabla \cdot \mathbf{v}\mathbf{I})\mathrm{d}t \tag{19}$$

By substituting the first Hamiltonian operator on the right-hand side into the integral symbol, the following equation can be obtained

$$\dot{\mathbf{v}}^s = \frac{G}{\rho}\int_0^t (\nabla^2 \mathbf{v} + \nabla\nabla \cdot \mathbf{v} - \frac{2}{d}\nabla\nabla \cdot \mathbf{v})\mathrm{d}t \tag{20}$$

When considering weakly compressible conditions, i.e., $\nabla \cdot \mathbf{v} \approx 0$, Eq. (20) can be simplified to

$$\dot{\mathbf{v}}^s \approx \frac{G}{\rho}\int_0^t (\nabla^2 \mathbf{v})\mathrm{d}t \tag{21}$$

It should be noted that, even for incompressible materials, the theoretical velocity divergence is zero but not necessarily numerically zero. Therefore, assuming the velocity divergence to be zero may introduce certain errors. Nevertheless, the results of extensive test cases in Section 6 exhibit strong agreement with both theoretical solutions and numerical results reported in literature, which suggests that the introduced error is not noticeable. The Laplacian operator needs to be discretized for calculating the shear acceleration. Refer to the literature [38], $\nabla^2 \mathbf{v}$ can be discretized as

$$\nabla^2 \mathbf{v} = 2\sum_j \frac{\mathbf{v}_{ij}}{r_{ij}}\frac{\partial W_{ij}}{\partial r_{ij}}V_j \tag{22}$$

However, the aforementioned formula does not fulfill the requirement for rigid rotational invariance. In other words, using this discretized form of the second derivative of velocity to compute shear acceleration in Eq. (21) cannot remove the effects of rigid rotation. Monaghan and Gingold [44] proposed the artificial viscosity in inviscid SPH considering the linear and angular momentum in 1993. Cleary et al. [45,46] discretized the viscous-force term similar to the artificial viscosity. Based on previous works [44–46], we adopt a discretization for the second derivative of velocity that conforms to the requirement of rigid rotational invariance, to eliminate the contribution of rigid rotation to the shear acceleration that should not have occurred in the first place, as shown in Eq. (23). It is important to note that while Eq. (23) exhibits local inconsistency due to the truncated kernel domains for surface particles, it does not affect global consistency, as theoretically proved by Colagrossi et al. [47].

$$\nabla^2 \mathbf{v} = 2\zeta\sum_j \frac{\mathbf{e}_{ij} \cdot \mathbf{v}_{ij}}{r_{ij}}\nabla_i W_{ij} V_j \tag{23}$$

where ζ is a positive parameter related to the smoothing length h and the type of kernel function [39]. ζ needs to be calibrated with numerical experiments. Through empirical calibration with solutions from known exact transient flow, Cleary [45] determined that the value of ζ is 4.96333. Cummins and Rudman [48] discovered that, when utilizing a pressure projection in incompressible SPH simulations of 2D flows, the parameter ζ is determined to be 4.167. Hu and Adams [39] assigned a value of $d+2$ (d is the spatial dimension) to the parameter ζ in SPH simulations of incompressible viscous flow. In this study, considering the chosen kernel type and smoothing length, the coefficient ζ is determined as $0.7d$+2.1 (3.5 for 2D scenarios and 4.2 for 3D scenarios) through numerical experiments conducted on 2D and 3D oscillating plates (section 6.1 and 6.2), alongside a comparison with theoretical values.

Then the non-nested formulation of shear acceleration can be written as

$$\frac{\mathrm{d}\mathbf{v}_i^s}{\mathrm{d}t} = 2\zeta \frac{G}{\rho_i} \int_0^t \left(\sum_j \frac{\mathbf{e}_{ij} \cdot \mathbf{v}_{ij}}{r_{ij}} \nabla_i W_{ij} V_j \right) \mathrm{d}t \tag{24}$$

Compared to original SPH methods, this formula is capable of eliminating zero energy modes, i.e., it can account for the variations in shear acceleration caused by the motion illustrated in Fig. 2. Eq. (24) is the final form of shear acceleration without hourglass modes, and thus can eliminate numerical instabilities in essence. It should be noted that the shear acceleration calculated at time step n will be used at the next time step $n+1$.

5. Dual-criteria time stepping

As we mentioned in Section 1, due to the necessity of updating particle configurations at each computational time step, a persistently challenging issue in ULSPH is its low computational efficiency. In this section, the dual-criteria time stepping originally proposed for fluid simulations [34] is introduced to solid simulations for the first time, to improve the calculation efficiency by reducing the frequency for updating particle configurations, while maintain high computation accuracy at the same time.

The dual-criteria time stepping strategy employs a larger advection time step $\triangle t_{ad}$, and a smaller acoustic time step $\triangle t_{ac}$. The particle configuration is updated in the advection time step $\triangle t_{ad}$, which is defined as

$$\triangle t_{ad} = CFL_{ad} \frac{h}{|\mathbf{v}|_{max}} \tag{25}$$

where $CFL_{ad} = 0.2$, $|\mathbf{v}|_{max}$ is the maximum particle advection speed and h is the smoothing length. The acoustic time step $\triangle t_{ac}$, involving the update of particle properties such velocity and density, has the following form

$$\triangle t_{ac} = CFL_{ac} \frac{h}{c_0 + |\mathbf{v}|_{max}} \tag{26}$$

where $CFL_{ac} = 0.4$ and c_0 is the sound speed.

Then the position-based Verlet scheme is applied for the acoustic time integration [49]. The beginning of the acoustic time step is indicated by superscript n, and the midpoint and new time step are donated by superscript $n+\frac{1}{2}$ and $n+1$ respectively. In the Verlet scheme, the particle position and density are firstly updated to the midpoint with

$$\begin{cases} \mathbf{r}^{n+\frac{1}{2}} = \mathbf{r}^n + \frac{1}{2}\triangle t_{ac}\mathbf{v}^n \\ \rho^{n+\frac{1}{2}} = \rho^n + \frac{1}{2}\triangle t_{ac}(\frac{\mathrm{d}\rho}{\mathrm{d}t})^n \end{cases} \tag{27}$$

Then the velocity is updated to the new time step after the particle acceleration is determined.

$$\mathbf{v}_{n+1} = \mathbf{v}_n + \triangle t_{ac}(\frac{\mathrm{d}\mathbf{v}}{\mathrm{d}t})^n \tag{28}$$

Finally, the particle position and density are updated to the new time step by

$$\begin{cases} \mathbf{r}^{n+1} = \mathbf{r}^{n+\frac{1}{2}} + \frac{1}{2}\triangle t_{ac}\mathbf{v}^{n+1} \\ \rho^{n+1} = \rho^{n+\frac{1}{2}} + \frac{1}{2}\triangle t_{ac}(\frac{\mathrm{d}\rho}{\mathrm{d}t})^{n+1} \end{cases} \tag{29}$$

All the physical variables are updated in the smaller acoustic time step $\triangle t_{ac}$, while the particle configuration (i.e., the neighbors of each particle) is updated in the larger advection time step $\triangle t_{ad}$. In this study, the advection time step $\triangle t_{ad}$ is approximately 5-10 times larger than the acoustic time step $\triangle t_{ac}$, with some variation depending on the material parameters and maximum velocity. Consequently, compared to the previous single time step method, the dual-criteria time stepping approach presented in this study can save 80%-90% of the time required for updating particle configurations.

6. Numerical examples

In this section, several benchmark cases are tested, and the results are compared with analytical solutions or the results from other numerical studies, from both qualitative and quantitative perspectives. Specifically, our results are compared with the results obtained using original SPH formulation and original formulation with artificial stress [7], to illustrate the calculation accuracy, stability, and robustness of the present method. Several abbreviations for different SPH methods are defined to facilitate the writing and reading of the article. The original SPH method is defined as “SPH-OG”; the original SPH method with introducing artificial stress [7] is represented by “SPH-OAS”; the present essentially non-hourglass formulation is expressed as “SPH-ENOG” in the following text. There are two artificial coefficients in the artificial stress term, and the selection of them refers to the literature [7] in this section.

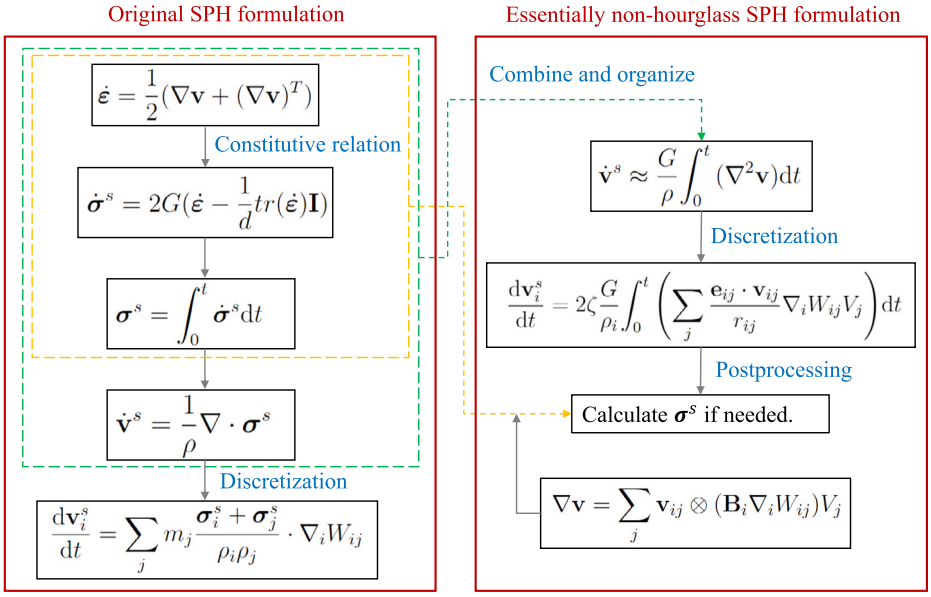

Fig. 3. Flowcharts of the original and the present essentially non-hourglass SPH formulations.

The 5th-order Wendland kernel [50] with a smoothing length of $h = 1.3dp$ and the cut-off radius equals to $2.6dp$, where dp is the initial particle spacing, is applied for all the cases in this paper. All the physical quantities in this article are presented in the dimensionless form.

In this newly-developed non-hourglass formulation, we skip the calculation of shear stress and the shear acceleration is computed directly. The shear stress can be obtained separately by Eq. (6)-Eq. (8) if needed. The velocity gradient in Eq. (8) is discretized by

$$\nabla \mathbf{v} = \sum_j \mathbf{v}_{ij} \otimes (\mathbf{B}_i \nabla_i W_{ij}) V_j \tag{30}$$

where $\mathbf{B}_i$ is the correction matrix for kernel gradient [19,51,52] and is defined as

$$\mathbf{B}_i = \left(\sum_j \mathbf{r}_{ij} \nabla_i W_{ij} V_j\right)^{-1} \tag{31}$$

To enhance clarity, Fig. 3 provides flowcharts delineating the calculation processes for the original and current SPH formulations. All the simulations in this section are run on a CentOS-8 system with 32 cores. The detail information of the CPU is “64 Intel(R) Xeon(R) Gold 6226R CPU @ 2.90GHz”.

6.1. 2D oscillating plate

As shown in Fig. 4, a 2D plate with one edge fixed is firstly used to verify the proposed method, and the results are compared with previous theoretical [53] and numerical [7] solutions. The length and thickness of the plate are L and H respectively, and the left part is fixed to produce a cantilever plate. Observation point-1 is set at the middle of the tail, and the vertical displacement of the point is recorded as the deflection, with upward being positive and downward being negative. Observation point-2 and Observation point-3 are used to measure the stress. An initial velocity v_y, which perpendicular to the plate strip, is applied with

$$v_y(x) = v_f c_0 \frac{f(x)}{f(L)} \tag{32}$$

where the constant v_f is an input parameter, c_0 is the sound speed as defined in Eq. (5) and

$$\begin{aligned} f(x) = {} & (\sin(kL) + \sinh(kL))(\cos(kx) - \cosh(kx)) \\ & -(\cos(kL) + \cosh(kL))(\sin(kx) - \sinh(kx)) \end{aligned} \tag{33}$$

where $kL = 1.875$ is determined by $\cos(kL)\cosh(kL) = -1$. The frequency ω of the oscillating plate is theoretically given by

$$\omega^2 = \frac{EH^2k^4}{12\rho_0(1-\nu^4)} \tag{34}$$

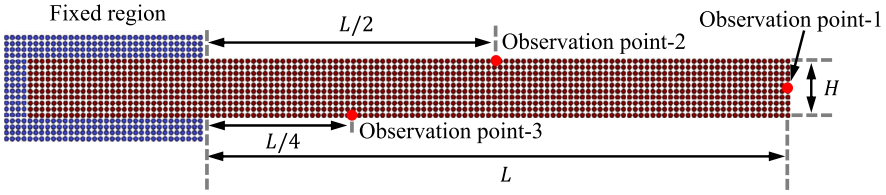

Fig. 4. Model setup for 2D oscillating plate.

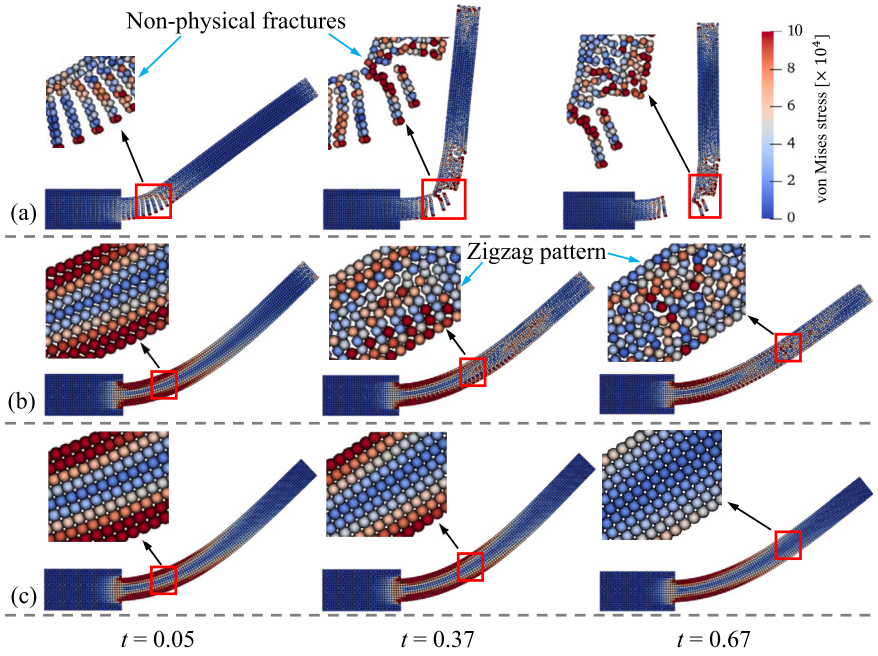

Fig. 5. Evolution of particle configuration with time (t = 0.05, 0.37 and 0.67) for (a) SPH-OG, (b) SPH-OAS, and (c) SPH-ENOG. The particles are colored by von Mises stress and $v_f = 0.05$.

The material and dimensional parameters in this case follow literatures [7,27], i.e., density $\rho_0 = 1000$, Young's modulus $E = 2 \times 10^6$, Poisson's ratio $\nu = 0.3975$, $L = 0.2$, and $H = 0.02$.

As shown in Fig. 5(a), SPH-OG leads to severe numerical instabilities (non-physical fractures and zigzag patterns in Fig. 1) when simulating elastic deformation. Numerical fractures occur at the beginning of the simulation ($t = 0.05$); the zigzag particle distribution and the non-uniform profile of von Mises stress indicate the hourglass modes. Fig. 5(b) shows the results obtained by SPH-OAS, in which the non-physical fractures can be suppressed. However, the zigzag patterns still occur and became visually evident when $t = 0.37$. This is because the error in the original formulation is in integral form, which gradually accumulates over time. The results produced by the present SPH-ENOG are shown in Fig. 5(c). Clearly, neither non-physical fractures and zigzag patterns appear even when the time $t = 0.67$. The particle distribution is still uniform, and the stress profile is smooth.

The convergence of the present new formulation is validated in Fig. 6. Three cases with different resolutions ($H/dp = 10$, $H/dp = 20$ and $H/dp = 30$) are tested and the variation of deflection and energy of the system over time are illustrated in Fig. 6a and Fig. 6b, respectively. It can be observed that, with the increase of resolution, the differences between different solutions are deceasing, which is consistent with the results in literatures [7,27,33,14] and indicates the convergence of this present algorithm. The theoretical values of the deflection over time are also depicted in Fig. 6a [14]. It is evident that as the resolution improves, the numerical results rapidly converge towards the theoretical values. Fig. 6b shows the variation of elastic strain energy, kinetic energy, and total energy with time for the present SPH-ENOG with $H/dp = 30$, while the theoretical solution for kinetic energy is also presented for ease of comparison. It can be observed that the calculated changes in kinetic energy align well with the theoretical values. Moreover, kinetic energy and elastic strain energy alternate changes, while their sum, the total energy, remains nearly constant, although there is a slight decrease in total energy throughout the process due to numerical dissipation.

Then a stress testing is performed with a long-time simulation, to check the stability of the current algorithm. As shown in Fig. 7, the simulation lasts for over 30 oscillations, and the result from SPH-OAS is also illustrated for comparison. Here, the two simulations are run with single time step [27], as we want to minimize the accumulated integration error in long-time simulations. The images above and below the curves in Fig. 7 respectively represent the particle distribution obtained using SPH-ENOG and SPH-OAS at a time around 10. As depicted in Fig. 7, with the proposed SPH-ENOG, the particle and stress distribution still keep uniform until the

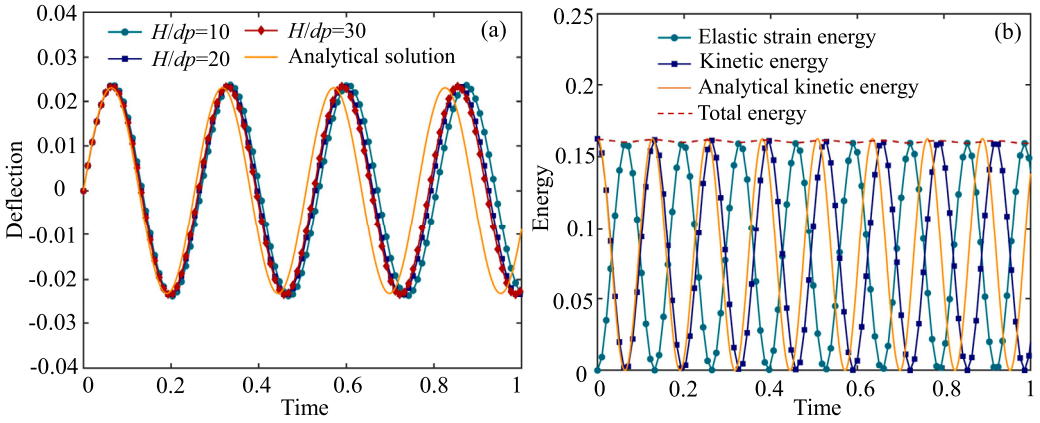

Fig. 6. Convergence verification for the 2D oscillating plate with the present SPH-ENOG: (a) The change of deflection with time; (b) the variation of elastic strain energy, kinetic energy, and total energy with time ($H/dp = 30$). Here, $L = 0.2$, $H = 0.02$, and $\mathbf{v}_f = 0.01$.

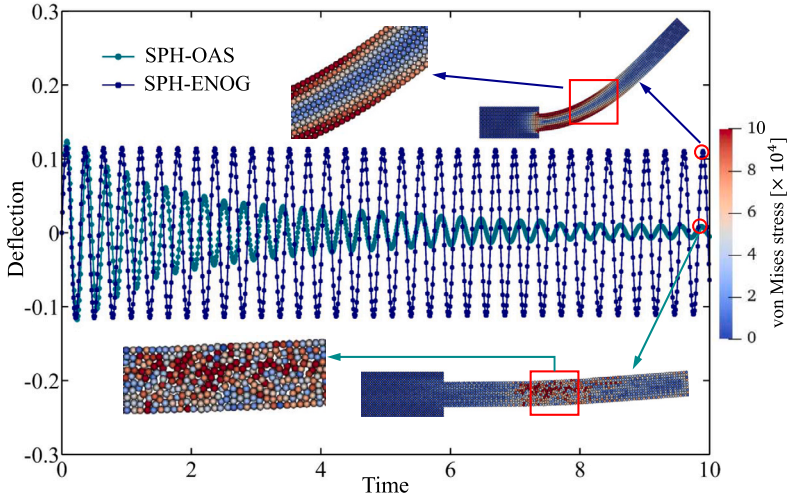

Fig. 7. Test the long-term stability for the SPH-ENOG, the result is compared with the SPH-OAS. Here, $L = 0.2$, $H = 0.02$, $H/dp = 10$ and $\mathbf{v}_f = 0.05$. The particles are colored by von Mises stress.

end of the simulation; while for SPH-OAS, the hourglass issue appears to be serious at $t \approx 10$. Moreover, with the present SPH-ENOG, the deflection only decreases marginally at t around 10 compared with the deflection at $t = 0$. The slight decrease in deflection over time is due to the numerical dissipation introduced in the Riemann solver [36]. On the contrary, the SPH-OAS exhibits rapid energy decay, thus it cannot be used for long-duration computations.

Furthermore, the accuracy is checked and verified with theoretical solutions and SPH-OAS from Gray et al.'s work [7]. As shown in Table 1, the first period of oscillation is recorded for both SPH-ENOG and SPH-OAS with $L = 0.2$, $H = 0.02$ and $H/dp = 30$. Compared with the analytical solution, the errors of the SPH-ENOG are at the same level as SPH-OAG, confirming the accuracy of the current SPH-ENOG. It should be noted that the analytical solution is obtained based on a thin plate model. If the thickness of the plate is reduced to $H = 0.01$, the error with $\upsilon_f = 0.001$ for the SPH-ENOG also decreases to around 0.6%, which is in consistent with previous studies [7,27].

The calculated stress of the present ULSPH-ENOG is verified with the ULSPH-OAS and TLSPH [33]. Fig. 8 shows the change of von Mises stress with the deflection increasing from zero to the maximum value for observation point-2 and point-3. We ran the code provided in reference [33] and obtained the results of TLSPH as a reference value. It can be observed that, at the lower deflection (0-0.01), the results of ULSPH-ENOG and ULSPH-OAS are close and both align well with the results of TLSPH. As the deflection increases (0.01-0.03), ULSPH-ENOG continues to match well with TLSPH results, while the discrepancy between ULSPH-OAS and TLSPH results gradually increases due to errors introduced by the hourglass.

Simultaneously, we provided visual evidence to demonstrate that the non-physical fractures occur after zigzag patterns (hourglass modes). As shown in Fig. 9, when we simulate the 2D oscillating plate using the SPH-OG, we first observe the appearance of zigzag patterns at the initial stage ($t = 0.012$), and non-physical fractures gradually emerge afterwards at $t = 0.021$. Additionally, the findings in Fig. 5c demonstrate that the elimination of hourglass modes also results in the disappearance of non-physical fractures, even in

Table 1
Comparison of oscillation periods T obtained from the present SPH-ENOG, SPH-OAS and analytical solutions. Here, $L = 0.2$, $H = 0.02$ and $H/dp = 30$.

v_f	0.001	0.01	0.03	0.05
T (Analytical)	0.254			
T (SPH-ENOG)	0.262	0.263	0.268	0.279
T (SPH-OAS)	0.273	0.273	0.275	0.278
Error (SPH-ENOG)	3.1%	3.5%	5.5%	9.8%
Error (SPH-OAS)	7.5%	7.5%	8.3%	9.4%

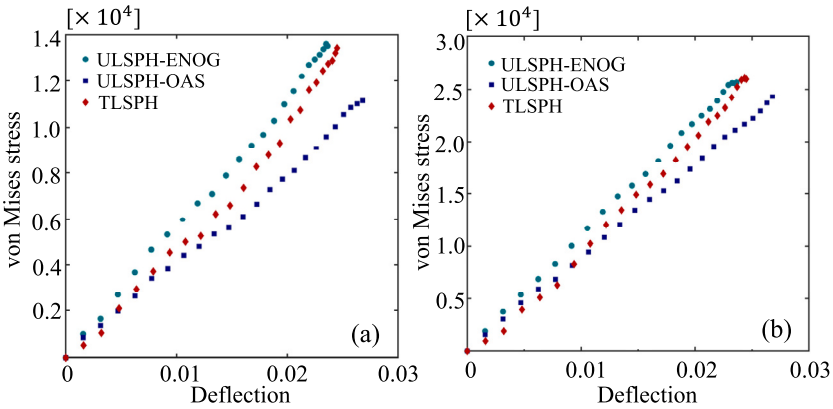

Fig. 8. The variation of von Mises stress as the deflection increases from zero to its maximum value for (a) observation point-2 and (b) observation point-3. Here, $L = 0.2$, $H = 0.02$, $H/dp = 10$ and $\mathbf{v}_f = 0.01$.

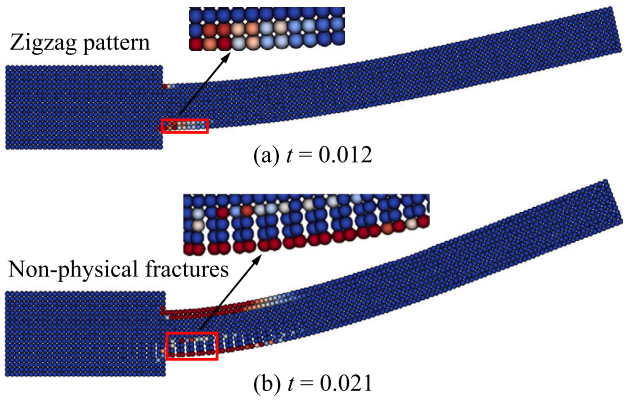

Fig. 9. Illustration for occurrences of zigzag pattern and non-physical fractures in 2D oscillating plates with the SPH-OG. The zigzag pattern appears at the initial stages when (a) $t = 0.012$, and the non-physical fractures can be observed later at (b) $t = 0.021$. The particles are colored by von Mises stress and $v_f = 0.05$.

regions subjected to notable tensile stresses. This suggests that, unlike in fluid dynamics, the non-physical fractures in elastodynamics are caused by the hourglass modes, or it is just another form of hourglass modes.

Next, we demonstrate the differences in computational results between adopting (Eq. (23)) or not adopting (Eq. (22)) rigid rotation-invariant formulations in discretizing the second derivative of velocity gradient. As shown in Fig. 10, it can be observed that when without the rigid rotation-invariant form, the behavior of the oscillating plate does not oscillate as expected, but exhibits a strong resistance to motion. This is because, the influence of rigid rotation is not eliminated in the non-conservative form, which means that rigid rotation can also produce significant shear forces, thereby hindering the plate's motion. Correspondingly, the behavior of the plate can be correctly estimated with the rigid rotation-invariant form.

The performance of dual-criteria time stepping scheme is tested with the SPH-ENOG, and the results from previous single time stepping method [27] are used for comparison. As shown in Table 2, the simulation ends at physical time $t = 1$, and the wall-clock time spent for dual-criteria (donate as T_d) and single-criteria (donate as T_s) time stepping is recorded. It can be seen the computing efficiency of the dual-criteria time steeping is approximately twice that of the previous method.

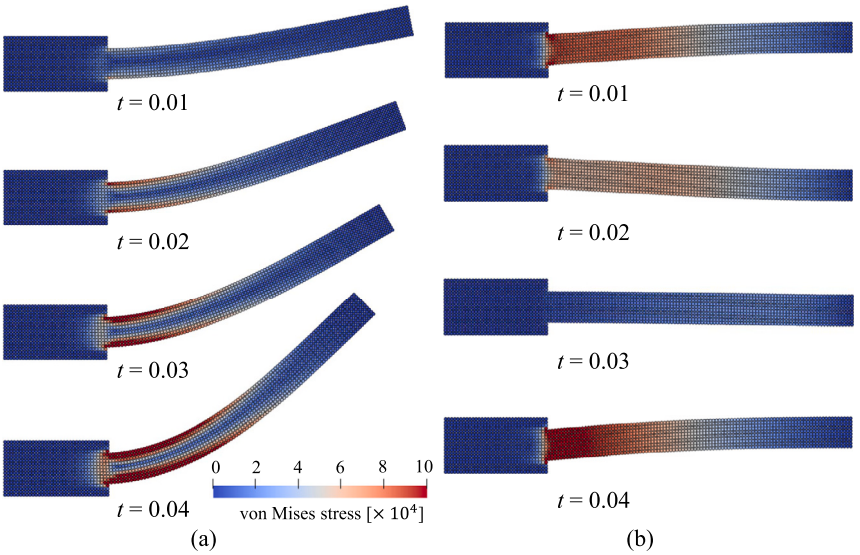

Fig. 10. Demonstration of the differences in the behavior of oscillating plates when discretizing the second derivative of velocity gradient with and without the rigid rotation-invariant formulation: (a) with the rigid rotation-invariant formulation; (b) without the rigid rotation-invariant formulation. Here, $L = 0.2$, $H = 0.02$, $H/dp = 10$ and $\mathbf{v}_f = 0.05$. The particles are colored by von Mises stress.

Table 2
Comparison of computational efficiency for dual-criteria (T_d) and single-criteria (T_s) time stepping scheme with the 2D oscillating beam. Here, $L = 0.2$, $H = 0.02$ and $\mathbf{v}_f = 0.05$. The simulation stops at physical time $t = 1$ and the wall-clock time spent is recorded. N_p represents the total particle number.

H/dp	10	20	30
N_p (k)	1.6	5.8	12.6
T_d	25.8	66.3	130.1
T_s	43.0	139.5	333.0

6.2. 3D oscillating plate

The oscillation of a 3D thin plate, with a simple support boundary condition for all lateral edges, is considered in this section. As shown in Fig. 11, a square plate with length $L = 0.4$, width $= 0.4$ and height $H = 0.01$ is constructed [13,33,54]. A simple boundary condition is applied to the particles in the middle of the four lateral sides. Specifically, the displacement of these particles along the z-direction is fixed. An observation point is set at the center of the plate to measure the deflection. The particles are subjected to the initial velocity v_z

$$v_z(x, y) = \sin\frac{m\pi x}{L}\sin\frac{n\pi y}{W} \tag{35}$$

where m and n donate integers controlling the vibration mode in x and y directions respectively. The theoretical vibration period for the 3D thin plate is given by

$$T = \frac{2}{\pi}\left[\left(\frac{m}{L}\right)^2 + \left(\frac{n}{W}\right)^2\right]^{-1}\sqrt{\frac{\rho_0 H}{D}} \tag{36}$$

where D represents the flexural rigidity and is defined as

$$D = \frac{EH^3}{12(1-\nu^2)} \tag{37}$$

The material parameters are set as follows: density $\rho_0 = 1000$, Young's modulus $E = 1 \times 10^8$, and Poisson's ratio $\nu = 0.3$.

Firstly, the particle distribution and the profile of von Mises stress are checked. Fig. 12 illustrates the deformed particle configuration with von Mises stress contour obtained by the SPH-ENOG at time $t = 0.01$ for vibration modes $(m, n) = (1, 1)$ and $(2, 2)$. The SPH-ENOG can generate a smooth stress profile without non-physical fractures and zigzag patterns. Fig. 13 shows the evolution of

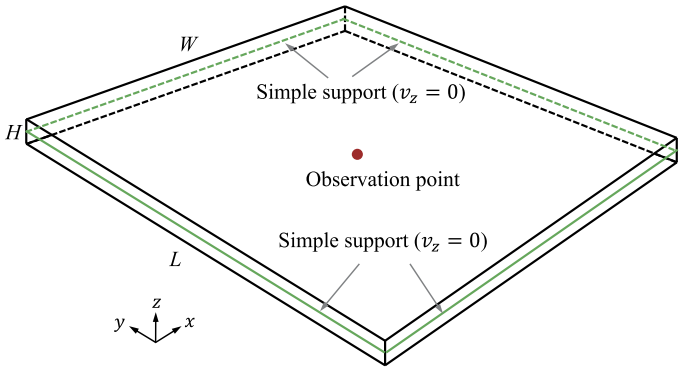

Fig. 11. Model setup for the 3D oscillating plate, and the observation point locates at the center of the plate.

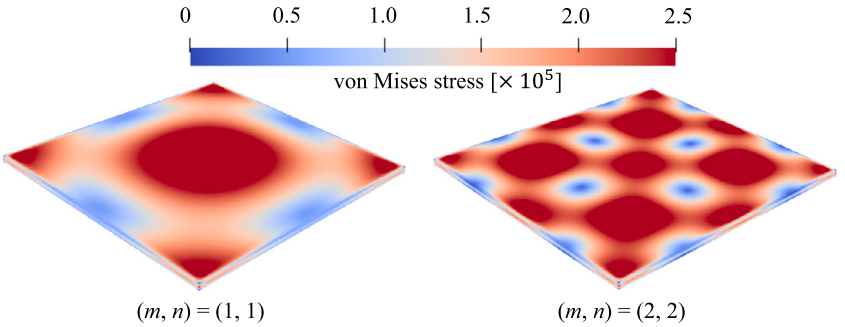

Fig. 12. 3D oscillating plates obtained by the SPH-ENOG at time $t = 0.01$ for vibration modes $(m, n) = (1, 1)$ and $(2, 2)$. The figures are colored by von Mises stress and the spatial particle discretization $H/dp = 9$.

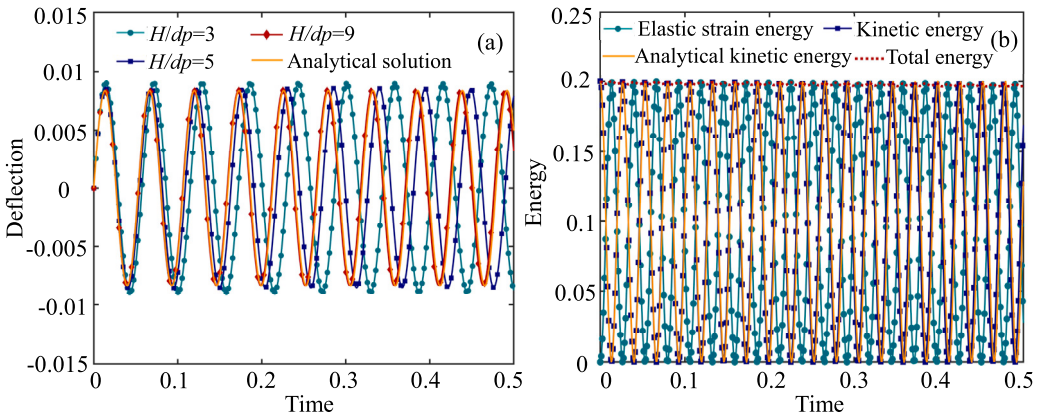

Fig. 13. Convergence verification for the 3D oscillating plate with the present SPH-ENOG: (a) The change of deflection with time; (b) the variation of elastic strain energy, kinetic energy, and total energy with time ($H/dp = 9$). Here, $(m, n) = (1, 1)$.

the deflection (displacement along z-axis of the observation point) and the system's energy with time. As can be seen in Fig. 13a, with the increase of resolution (decrease of initial particle spacing dp), the deflection and gradually approach the analytical solutions, indicating the convergence of the SPH-ENOG. Fig. 13b illustrates a good agreement between the calculated kinetic energy and the theoretical values with $H/dp = 9$. The elastic strain energy and kinetic energy alternate, while the total energy remains relatively constant. Moreover, the first periods of oscillations with different (m, n) values and resolutions are calculated and compared with analytical solutions, to further validate the convergence and accuracy of the present SPH-ENOG. As shown in Table 3, the periods converge rapidly with increasing resolutions and agree well with the analytical solutions.

The performance of dual-criteria time stepping scheme is tested with the SPH-ENOG for 3D oscillating plates, and the results from previous single time stepping method is used for comparison. As shown in Table 4, the simulation ends at physical time $t = 0.1$, and the wall-clock time spent for dual-criteria (donate as T_d) and single-criteria (donate as T_s) time stepping is recorded. Clearly, when

Table 3
Comparison of the first oscillation period T obtained the present SPH-ENOG and analytical solutions.

SPH-ENOG	$H/dp=3$	$H/dp=5$	$H/dp=9$	Analytical
$(m,n)=(1,1)$	0.0572	0.0543	0.0529	0.0532
$(m,n)=(2,1)$	0.0231	0.0218	0.0212	0.0213
$(m,n)=(2,2)$	0.0148	0.0140	0.0136	0.0133

Table 4
Comparison of computational efficiency for dual-criteria (T_d) and single-criteria (T_s) time stepping scheme with the 3D oscillating beam. Here, $(m,n)=(2,2)$. The simulation stops at physical time $t=0.1$ and the wall-clock time spent is recorded. N_p represents the total particle number.

H/dp	3	5	9
N_p (k)	44.7	204.0	1179.4
T_d	122.6	981.3	10629.4
T_s	331.2	2683.1	30273.3

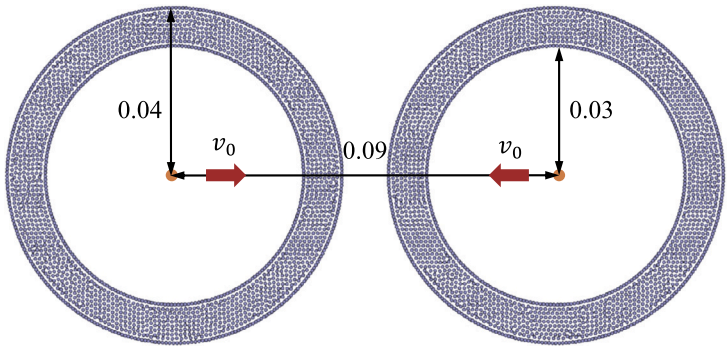

Fig. 14. Model setup for 2D colliding rubber rings.

using the dual-criteria time stepping approach, the computational time reduces to approximately one-third of the time required for single-criteria time stepping.

6.3. 2D colliding rubber rings

The collision of two rubber rings is simulated in this section refer to literatures [7,17,27]. As shown in Fig. 14, two rings with inner radius 0.03 and outer radius 0.04 are moving towards each other with the initial velocity magnitude v_0 (the relative velocity of the two rings is $2v_0$), and the distance between the centers of the two rings is 0.09. The initial uniform particle distribution is achieved by a level-set based pre-processing technique [55]. We employ an irregular initial particle distribution to address a generic scenario. The choice of an irregular distribution is made to avoid the simplification inherent in a radial particle distribution [27], especially when dealing with complex geometries. When two rings collide with each other, a significant tensile force will be generated. In this case, we will show that the numerical fracture produced by SPH-OG and the zigzag particle/stress distribution produced by SPH-OG and SPH-OAS do not occur in the present SPH-ENOG. The material parameters are set as follows: density $\rho_0=1200$, Young's modulus $E=1\times10^7$, and Poisson's ratio $\nu=0.4$. The initial particle spacing is 0.001.

Fig. 15 shows the evolution of particle configuration for the SPH-OG, SPH-OAS and the present SPH-ENOG when the initial velocity magnitude $v_0=0.06c_0$. Clearly, the SPH-OG suffers from serious non-physical fractures and zigzag patterns at the beginning of the computation ($t=0.002$), and the calculation process can barely continue. For the SPH-OAS, the non-physical fractures can be suppressed, and the particle distribution is uniform at the initial stage (t = 0.002). However, with the passage of time, the zigzag distribution of particle configuration and von Mises stress gradually becomes apparent. Note that, similar zigzag stress distribution can also be observed from the simulation using the recent tensile instability control (TIC) scheme [31] even with vary regular initial particle distribution (see Figs. 20 and 24 in reference [31]). While for the SPH-ENOG, the particle and stress distribution are uniform during the whole calculation process, and the numerical instabilities can be completely removed.

Fig. 16 illustrates the variation of elastic strain energy, kinetic energy, and total energy over time for the left (represented by solid lines) and right (represented by dots) rings. The stress distribution of rings at different time points ($t=0.002, 0.005$ and 0.01) is also illustrated. Firstly, it can be observed that the energy variation trends of the left and right rings are completely identical. To sum up,

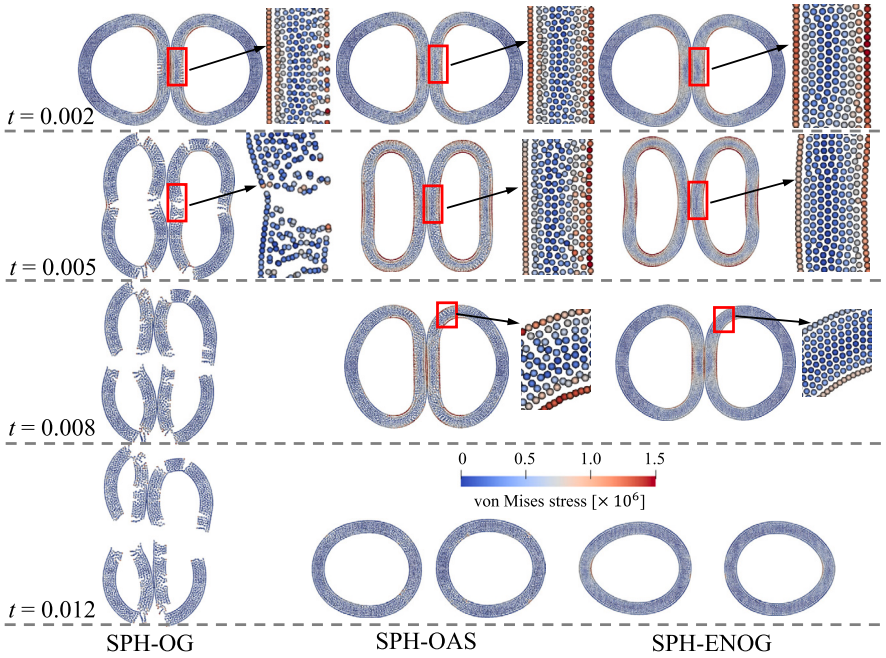

Fig. 15. Evolution of particle configuration with time ($t = 0.002$, 0.005, 0.008 and 0.012) for 2D colliding rubber rings. The results are obtained by different SPH methods, i.e., SPH-OG (left column), SPH-OAS (middle column), and SPH-ENOG (right column). The initial velocity magnitude $v_0 = 0.06c_0$ and the figures are colored by von Mises stress.

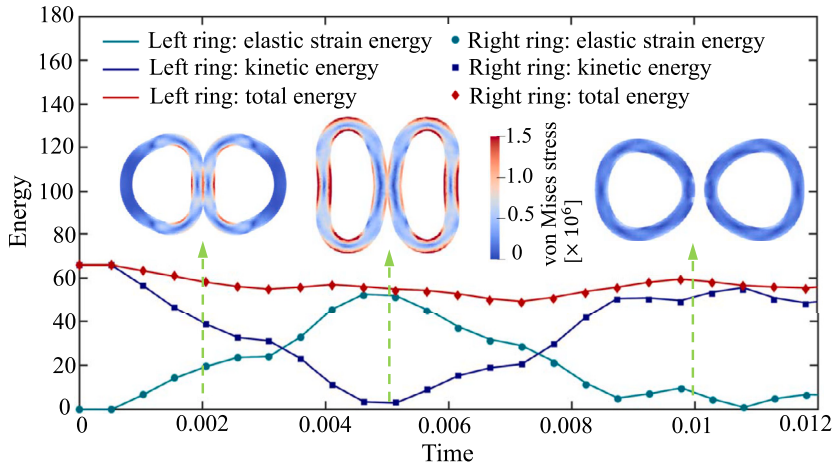

Fig. 16. The variation of elastic strain energy, kinetic energy, and total energy over time for the left (represented by solid lines) and right (represented by dots) rings. The distributions of von Mises at $t = 0.002, 0.005$ and 0.01 are also illustrated. The initial velocity magnitude $v_0 = 0.06c_0$.

while experiencing occasional fluctuations, the overall energy diminishes progressively over time, dropping from the initial value of 65.88 to 55.61 at the conclusion of the simulation. Simultaneously, it's noticeable that kinetic energy undergoes a swift reduction shortly after the collision of the two rings, reaching its minimum value at approximately $t = 0.005$. Following this, with the gradual separation of the two rings, kinetic energy gradually ascends, in stark contrast to the complete reversal observed in the change of elastic strain energy.

Then we increase the initial velocity v_0 to $0.07c_0$, to test the stability and robustness of the present SPH-ENOG. As shown in Fig. 17, the non-physical fractures and zigzag patterns become more significant for the SPH-OAS, compared with Fig. 15 when $v_0 = 0.06c_0$. Particularly, after the collision and rebound of the two rings ($t = 0.012$), the zigzag distribution of particles cannot be restored, indicating that this accumulated integration error over time is significant. On the contrary, the present SPH-ENOG can produce a uniform particle and stress distribution throughout the entire process.

Furthermore, the initial velocity is increased to $v_0 = 0.08c_0$. It can be seen from Fig. 18, not only zigzag patterns, but also numerical fractures appear when $t \geqslant 0.005$ for the SPH-OAS. Fortunately, the present SPH-ENOG performs well even at such large

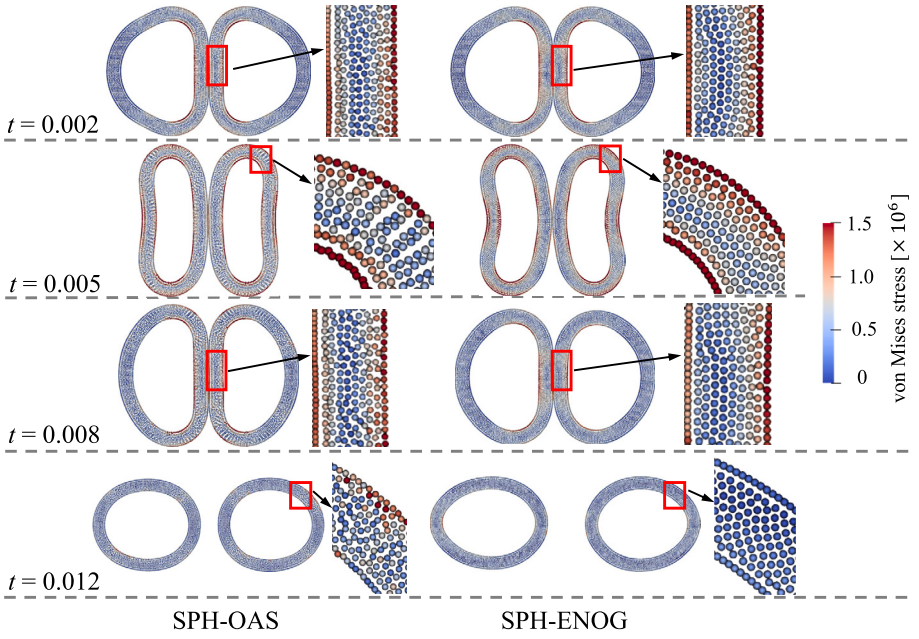

Fig. 17. Evolution of particle configuration with time ($t = 0.002$, 0.005, 0.008 and 0.012) for 2D colliding rubber rings. The results are obtained by different SPH methods, i.e., SPH-OAS (left column) and SPH-ENOG (right column). The initial velocity $v_0 = 0.07c_0$ and the figures are colored by von Mises stress.

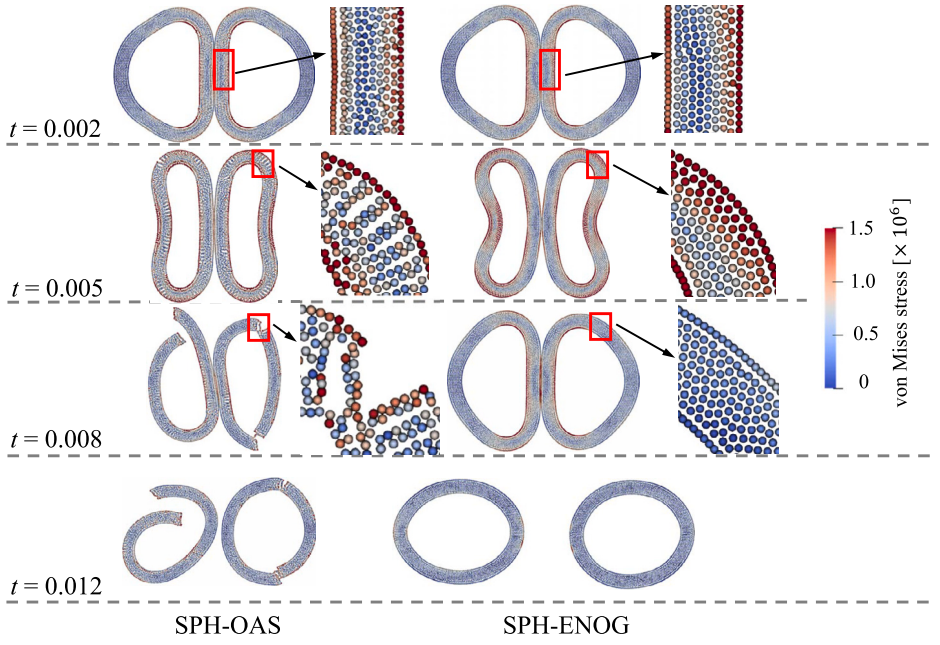

Fig. 18. Evolution of particle configuration with time ($t = 0.002$, 0.005, 0.008 and 0.012) for 2D colliding rubber rings. The results are obtained by different SPH methods, i.e., SPH-OAS (left column) and SPH-ENOG (right column). The initial velocity $v_0 = 0.08c_0$ and the figures are colored by von Mises stress.

initial velocity, and all numerical instabilities can be perfectly eliminated, which suggests the stability and robustness of the present SPH-ENOG.

6.4. 3D colliding rubber balls

The 2D colliding rubber rings are extended to 3D to validate the proposed SPH-ENOG for 3D scenarios. The initial setup follows Fig. 19, i.e., two hollow rubber balls with inner radius 0.03 and outer radius 0.04 are moving towards each other. The initial distance between the centers of the two balls is 0.09 and the initial velocity magnitude for each ball is v_0. The initial particle spacing

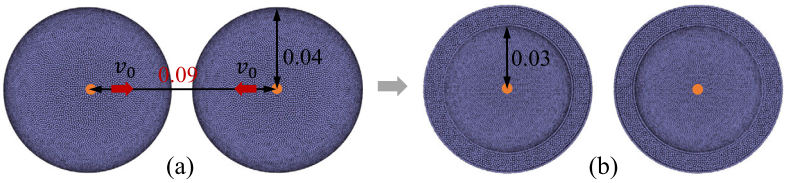

Fig. 19. Model setup for (a) 3D colliding hollow rubber balls and (b) the half of each ball are showcased for proper visualization.

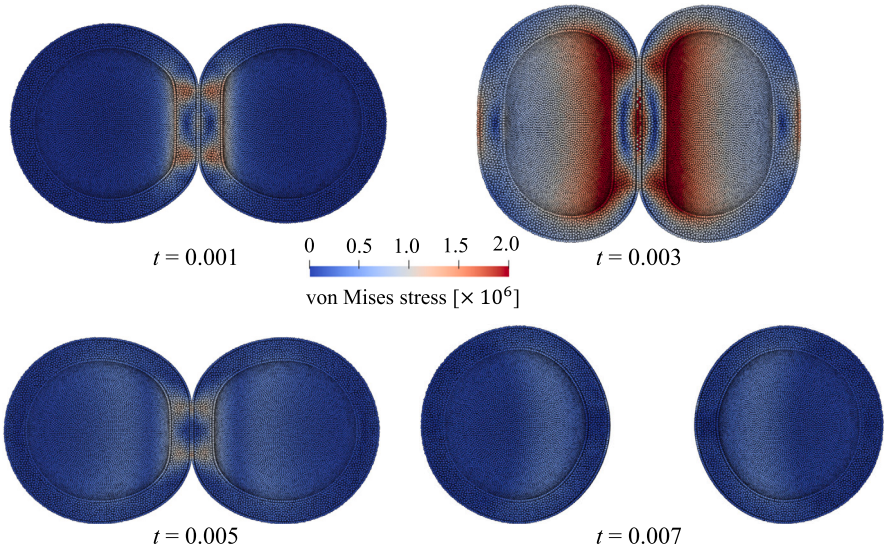

Fig. 20. Evolution of particle configuration with time ($t = 0.001$, 0.003, 0.005 and 0.007) for 3D colliding rubber balls. The results are obtained by the present SPH-ENOG. The initial velocity magnitude $v_0 = 0.08c_0$ and the figures are colored by von Mises stress.

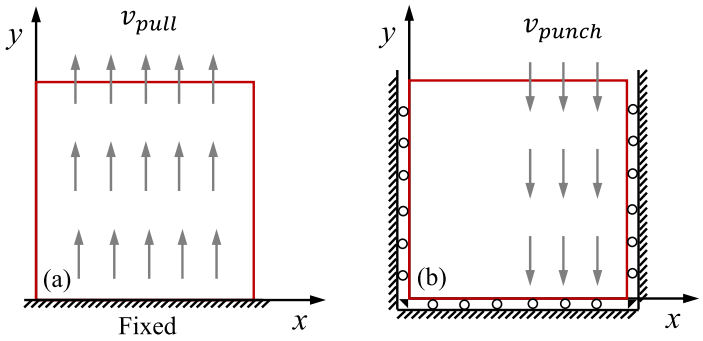

Fig. 21. Setup for (a) a tensile test and (b) a punch test.

$dp = 0.001$ and the uniform particle distribution at the beginning is realized by Yu et al.'s method [55]. The selection of material parameters follows section 6.3.

Fig. 20 shows the collision process of two balls at different times ($t = 0.001$, 0.003, 0.005 and 0.007) with the present SPH-ENOG. The initial velocity is set as $v_0 = 0.08c_0$. Half of each ball is displayed separately here for proper visualization. Obviously, the distribution of von Mises stress is smooth, and the particle configuration is uniform, which means numerical fractures and zigzag patterns can be completely removed.

6.5. A tensile test

We examine a case dominated by tensile stresses [10] to evaluate the effectiveness of the algorithm proposed in this study in eliminating numerical instabilities. As illustrated in Fig. 21a, a square plate with dimensions of 1×1, fixed at its bottom edge, is subjected to rapid upward stretching with a substantial velocity $v_{pull} = 500$. Refer to Lee et al. [10], the material parameters are defined as follows: density $\rho_0 = 7000$, Young's modulus $E = 2.1 \times 10^{10}$, and Poisson's ratio $\nu = 0.3$.

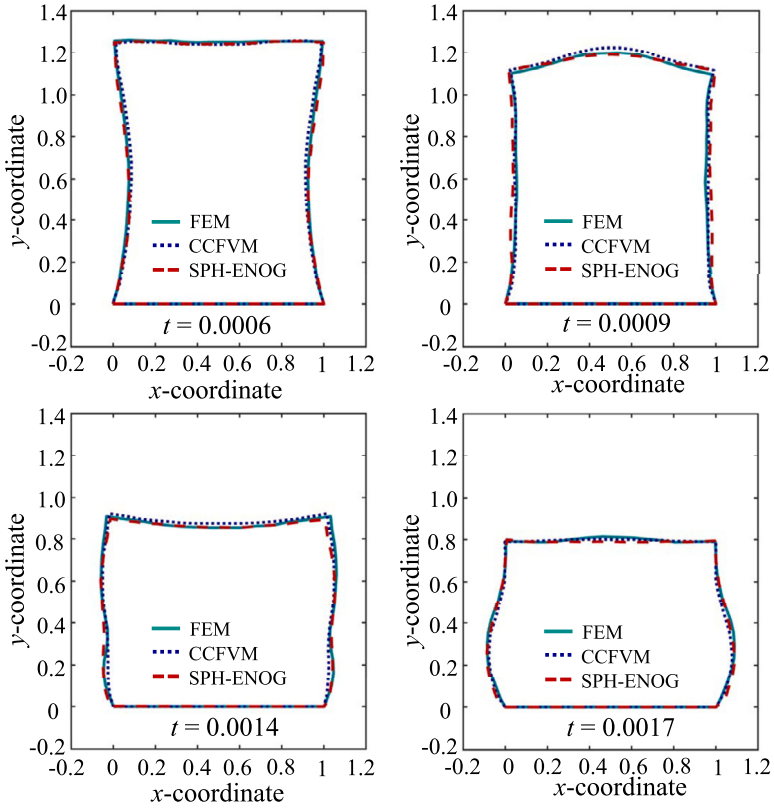

Fig. 22. Sequence of deformed shapes for the tensile test case using FEM [10], CCFVM [10] and the present SPH-ENOG. The initial particle spacing is 1/15.

Fig. 22 depicts the shape changes of the square plate at different time points. Additionally, results obtained from standard Finite Element Method (FEM) and cell centred Finite Volume Method (CCFVM) as presented in literature [10] are showcased for comparison. The initial particle spacing is 1/15 according to Lee et al. [10]. Under these circumstances, the results from FEM are deemed reliable and serve as a reference solution. Observably (Fig. 22), akin to the outcomes from CCFVM [10], the results obtained from the present SPH-ENOG align well with those from FEM. This indicates the accuracy of the proposed algorithm in addressing cases dominated by tensile stress. Fig. 23 shows the stress distribution of the square plate at different times ($dp = 0.025$ [10]). Notably, neither non-physical fractures nor zigzag patterns have occurred, underscoring the robust effectiveness of our algorithm even in scenarios where tensile stress prevails.

6.6. A punch test

We present a punch test case [10] wherein a flat square rubber plate with a side length of one unit is fixed using rollers positioned at the bottom and on both the left and right sides. The prescribed punch velocity, $v_{punch} = 100$, is applied to the right half of the domain, as shown in Fig. 21b. The material parameters are defined as follows [10]: density $\rho_0 = 1100$, Young's modulus $E = 1.7 \times 10^7$, and Poisson's ratio $\nu = 0.45$.

Fig. 24 showcases the shapes of the square at different time instants, along with the results from standard FEM and CCFVM [10] for comparison. It can be observed that although there are certain deviations compared to the results obtained from the grid-based method, the overall variation trend remains consistent. Additionally, a key focus of this case study is to demonstrate that the proposed method can achieve a smooth pressure distribution. The occurrence of volumetric locking is a widely recognized challenge in standard FEM analysis for almost incompressible rubber materials. In order to mitigate this issue, the mean dilatation approach is commonly adopted. However, regrettably, the results obtained using such approach often exhibit spurious pressure modes [10]. The present formulation, as illustrated in Fig. 25a, effectively addresses this issue, ensuring a smooth pressure distribution where positive values represent compression. A uniform distribution of von Mises stress (Fig. 25b) confirms that the present method can eliminate hourglas modes.

6.7. 2D rubber ball-plate interaction

Another interesting problem with large deformations and tensions produced is simulated in this section. As shown in Fig. 26a, a rubber ball with a radius of 0.05 is used to impact a rubber plate [27]. The plate, fixed at both ends, has dimensions of 0.5 in

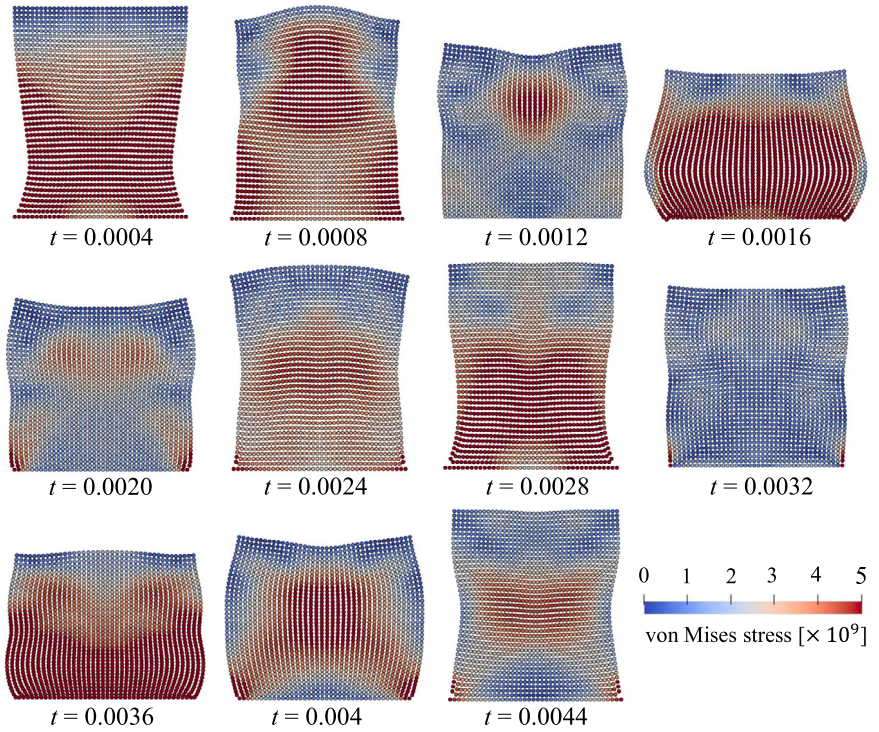

Fig. 23. Evolution of von Mises stress with time for the tensile test case. The initial particle spacing is 0.025.

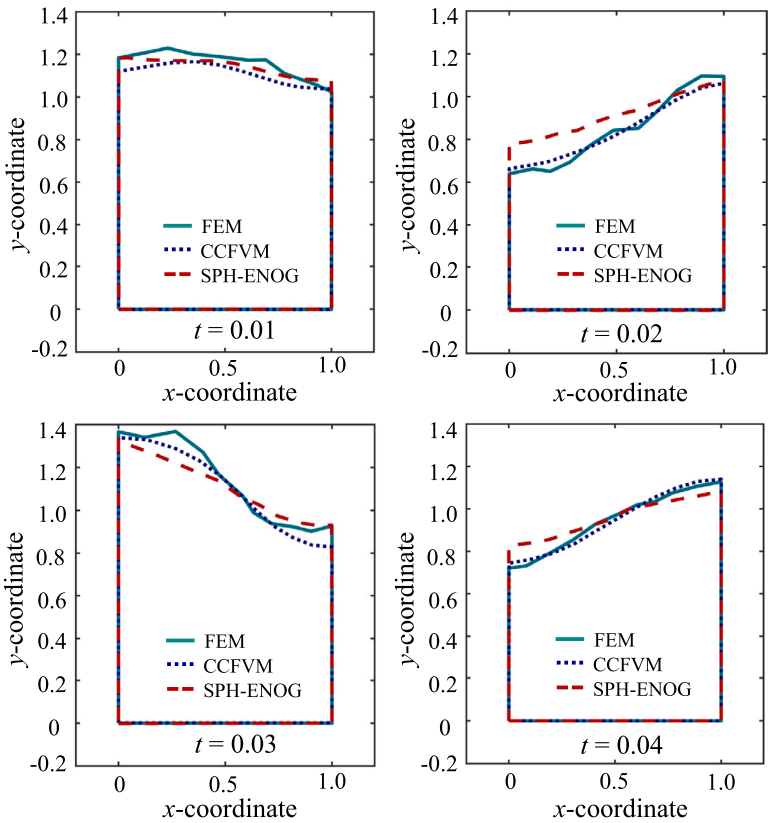

Fig. 24. Sequence of deformed shapes for the punch test using standard FEM [10], CCFVM [10] and the present SPH-ENOG. The initial particle spacing is 0.1.

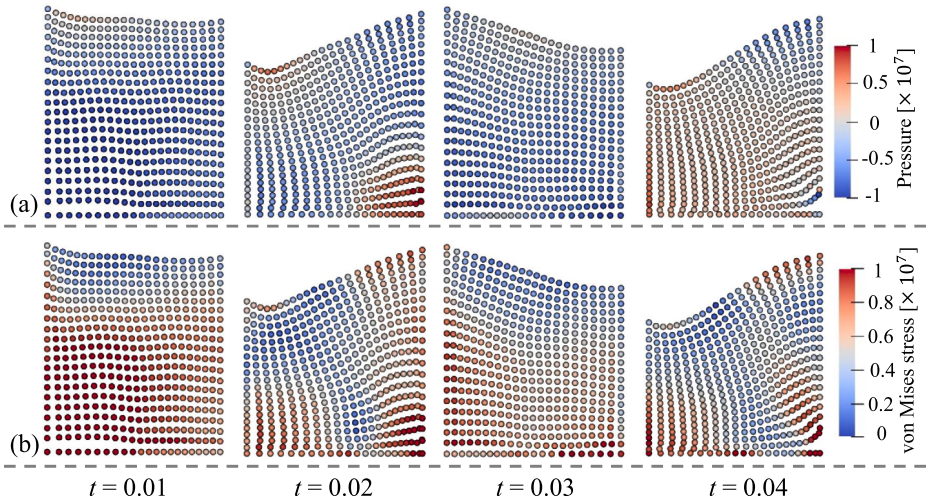

Fig. 25. Evolution of (a) pressure and (b) von Mises stress with time for the punch test. The initial particle spacing is 0.05.

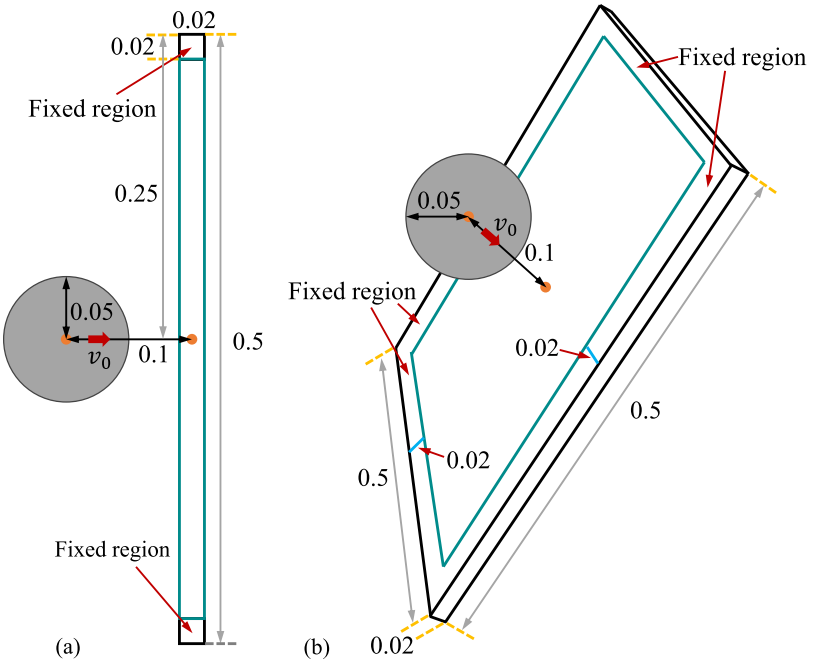

Fig. 26. Model setup for (a) 2D rubber ball-plate interaction, and (b) 3D rubber ball-plate interaction.

length and 0.02 in width. The center of the ball is located 0.1 units away from the center of the plate, and the initial velocity of the rubber ball is v_0. The material parameters of the rubber ball and the target plate are the same [27], i.e., density $\rho_0 = 1200$, Young's modulus $E = 1 \times 10^7$, and Poisson's ratio ν is set as 0.49 to produce a large deformation, mimicking realistic rubber materials. The initial particle spacing is 0.0025.

Fig. 27 illustrates the process of collision between the rubber ball and the target plate with an initial velocity of $0.02c_0$. Significant tensions will be generated on the plate after the ball touches it. Serious zigzag particle distribution and numerical fractures can be observed when using the SPH-OG (Fig. 27a). For the SPH-OAS (Fig. 27b), the numerical fractures can be suppressed but the zigzag pattern still exists. While with the present SPH-ENOG (Fig. 27c), the numerical fractures and zigzag patterns can be removed simultaneously. The phenomena are consistent with the results from the oscillating plate and colliding rubber rings/balls described in Section 6.1 and Section 6.3.

Afterwards, we increase the initial velocity of the ball ($v_0 = 0.06c_0$) to test the stability and applicability of the SPH-OAS and SPH-ENOG under a more demanding condition. It can be seen that the zigzag pattern still exists for the SPH-OAS (Fig. 28a), and to make matters worse, the numerical fractures start to appear at $t = 0.012$ and become very severe later. However, our method (Fig. 28b) still performs well under such condition, and numerical instabilities do not occur.

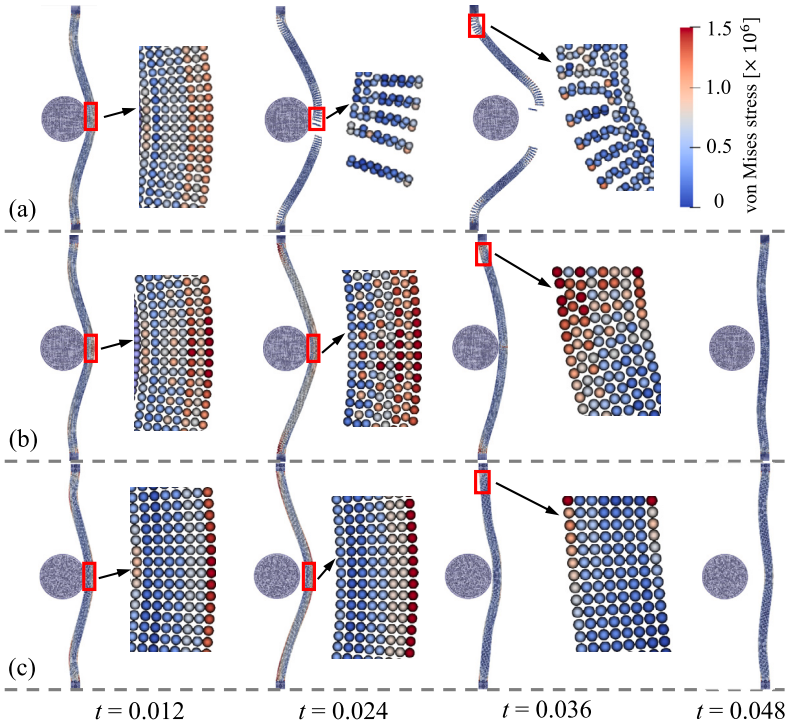

Fig. 27. 2D rubber ball-plate interaction with initial ball velocity $0.02c_0$ at different times. The results are obtained by (a) SPH-OG, (b) SPH-OAS and (c) SPH-ENOG respectively. The figures are colored by von Mises stress.

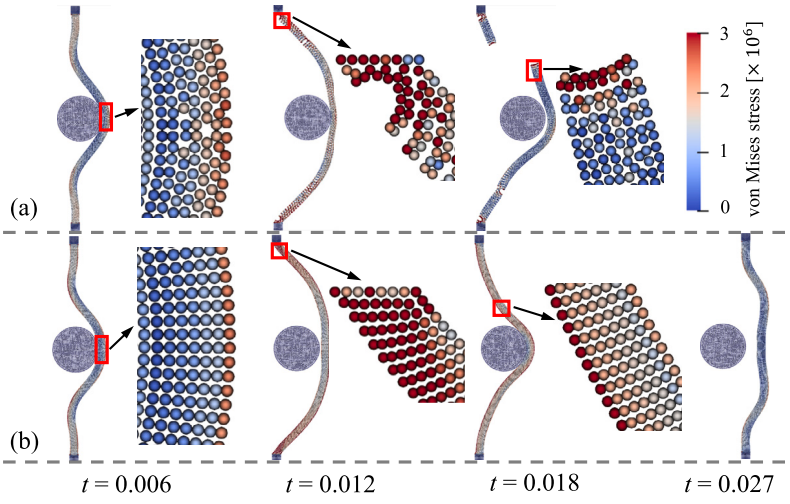

Fig. 28. 2D rubber ball-plate interaction with initial ball velocity $0.06c_0$ at different times. The results are obtained by (a) SPH-OAS and (b) SPH-ENOG respectively. The figures are colored by von Mises stress.

To further challenge the proposed SPH-ENOG, the initial velocity is set to $v_0 = 0.12c_0$ and extremely large tensions will be generated under such condition. As shown in Fig. 29, surprisingly, the particle configuration still keeps a uniform distribution and a smooth stress profile can be obtained, implying the robustness and stability of the current SPH-ENOG.

6.8. 3D rubber ball-plate interaction

We further consider the collision of the rubber ball and plate in 3D situations, as shown in Fig. 26b. The plate with a size of $0.5 \times 0.02 \times 0.5$ is fixed on all four edges. The line connecting the center of the ball and the center of the plate is perpendicular to the plane of the plate, and the direction of initial velocity v_0 lies along this line. The materials of the rubber ball and plate follow section 6.7, and the initial particle spacing is 0.0025.

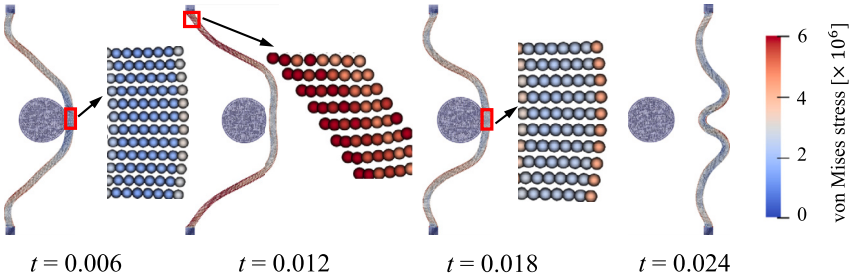

Fig. 29. 2D rubber ball-plate interaction with initial ball velocity $0.12c_0$ at different times. The results are obtained by the present SPH-ENOG and the figures are colored by von Mises stress.

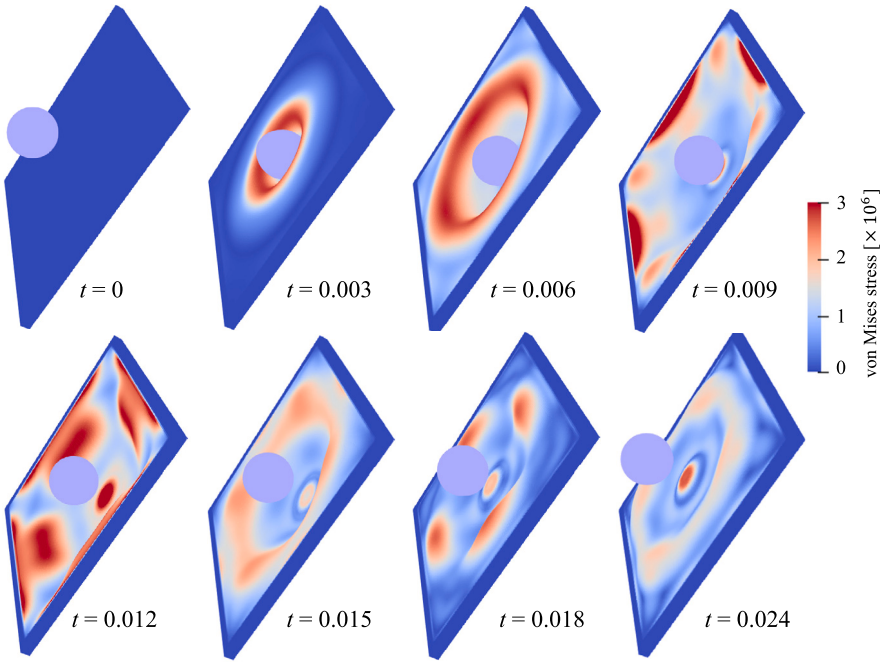

Fig. 30. 3D rubber ball-plate interaction with initial ball velocity $0.12c_0$ at different times. The results are obtained by the present SPH-ENOG and the figures are colored by von Mises stress.

The results with the SPH-ENOG and $v_0 = 0.12c_0$ are shown in Fig. 30. The profile of von Mises stress is smooth throughout the calculation process and there are no occurrences of numerical fractures. This demonstrates the capability of the present SPH-ENOG in eliminating numerical instabilities (numerical fractures and zigzag patterns) for 3D situations.

6.9. Bouldery debris flow impacting flexible barrier

In this section, a more complicated case, intricately linked to practical engineering application, is employed to validate the robustness of the algorithm proposed in this paper.

In mountainous areas, flexible steel net barriers are frequently employed to alleviate geological risks such as rockfall and debris flow occurrences [56,57]. Within the debris flow mass, natural boulders or sizable hard inclusions are widespread, tending to accumulate at the forefront of the flow [58]. The interaction between bouldery debris flows and flexible barriers are simulated in this section, and the model setup follows a previous experimental study [57].

As shown in Fig. 31, the simulation initiates with the removal of the rigid plate, followed by the release and sliding of the initial deposit of bouldery debris flows on the baseplate. Bouldery debris flows are simulated using solid particles with different sizes, and eventually, they come to a halt in front of the flexible barrier, causing significant deformation of the barrier as well. The movement and deformation of both debris flows and the barrier are computed using the algorithm proposed in this paper, while our primary focus is on the flexible barrier in this particular case, as it exhibits significant deformation. Refer to the experimental setup [57], a layer of membrane is placed on the upstream surface of the flexible barrier, serving as a net-like structure to obstruct and detain debris flow materials. Differing from the experimental setup, we removed the transverse rigid support within the barrier to induce greater deformation of the barrier, challenging the algorithm proposed in this study. The length and width of the baffle are both 4.5

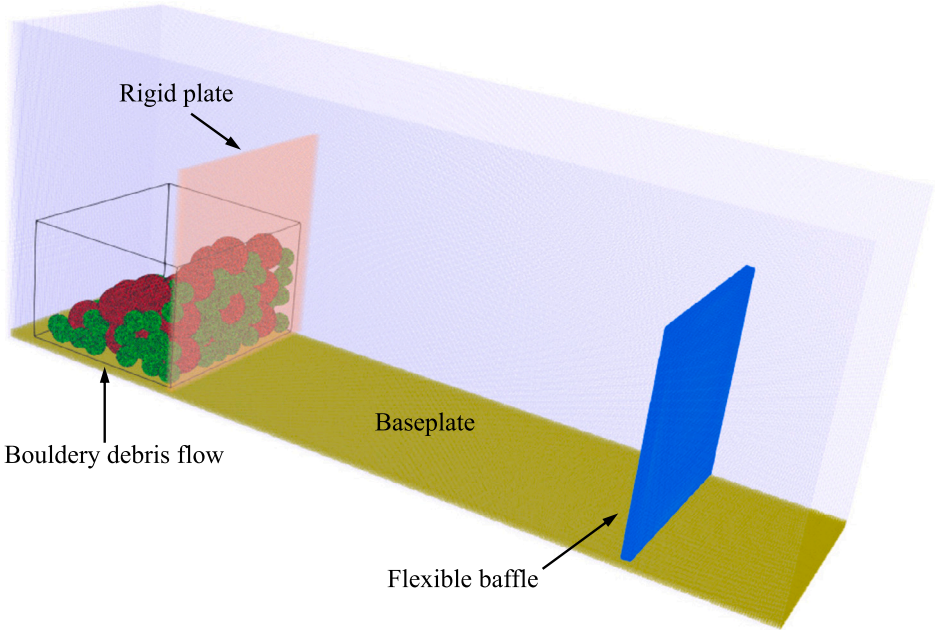

Fig. 31. Model setup for simulating the impact of bouldery debris flows on flexible barriers.

[57], and the distance between the rigid plate and baffle is 10.5. The density and Young's modulus of the debris flow materials are 2500 and 1×10^{10} respectively according to the physical testing [57], and the Poisson's ratio is set to 0.2. For the flexible baffle, the density, Young's modulus and Poisson's ratio are set to 1200, 1×10^{7} and 0.47 in this case. The angle between the baseplate and the horizontal plane is 30 degrees.

As depicted in Fig. 32, the simulation outcomes reveal the movement of the debris flow initiated by gravity, culminating in its collision with the barrier, inducing substantial deformation of the latter. Observably, our algorithm demonstrates stable performance even under intricate scenarios. Furthermore, the stress distribution on the barrier is uniform and smooth, with no occurrences of numerical instabilities, which is crucial for accurately simulating the elastic deformation phase prior to material failure.

6.10. Spinning plate

In Section 6.1-6.9, we demonstrate the stability and accuracy of the proposed method through multiple case studies. However, in certain cases that are highly sensitive to angular momentum, although the present formulation still obtains regular particle distribution and smoothed stress profile without numerical instability, it may not yield as accurate result as expected. This is due to the proposed formulation for shear acceleration does not strictly satisfy angular momentum conservation (while linear momentum is conserved). Although the discretized form of the second derivative of velocity (Eq. (23)) ensures angular momentum conservation, integrating it over time (Eq. (24)) leads to deviation of total angular momentum. Here, we begin with simulating a case known as the spinning plate [10], to illustrate the issue of angular momentum conservation. Subsequently, we provide a mathematical explanation for it.

The setup for the spinning plate is given in Fig. 33. A square plate with a side length of one rotates around its center without any initial deformation or constraints, with an angular velocity of $\omega = 50$. The material parameters are set as follows according to [10]: density $\rho_0 = 1100$, Young's modulus $E = 1.7 \times 10^{7}$, and Poisson's ratio $\nu = 0.45$. An observation point is placed at the top-right corner of the plate to measure the displacement and velocity.

Fig. 34 illustrates the configuration of the square and the temporal evolution of the pressure distribution. Fig. 35 depicts the variation of certain physical quantities during the computational process. While non-physical fractures and zigzag modes do not occur, it can be seen that the velocity variation (Fig. 35b) at the observation point is inaccurately estimated. Specifically, the velocity does not return to its initial value when the square returns to its initial position. This discrepancy arises from the lack of angular momentum conservation (while linear momentum is conserved), as illustrated in Fig. 35c. The variation in angular momentum also results in considerable deviations of the system's kinetic energy and total energy, as depicted in Fig. 35d.

Next, we will explain why integrating Eq. (23), which guarantees conservation of angular momentum, over time (Eq. (24)) results in the loss of angular momentum conservation. We will illustrate this through a simple scenario. As shown in the Fig. 36, four particles are positioned at the four corners of a square and rotate around the center of the square, spanning from time t_0 ($t_0 = 0$) to time t_1. Theoretically, the angular momentum of each particle is conserved, indicating that the net torque $\tau = \mathbf{x} \times \mathbf{F} = m\mathbf{x} \times \mathbf{a}$ exerted on them should be zero. Here, $\mathbf{x}$ is the position vector, $\mathbf{F}$ is the total force, m is mass, and $\mathbf{a}$ is the acceleration.

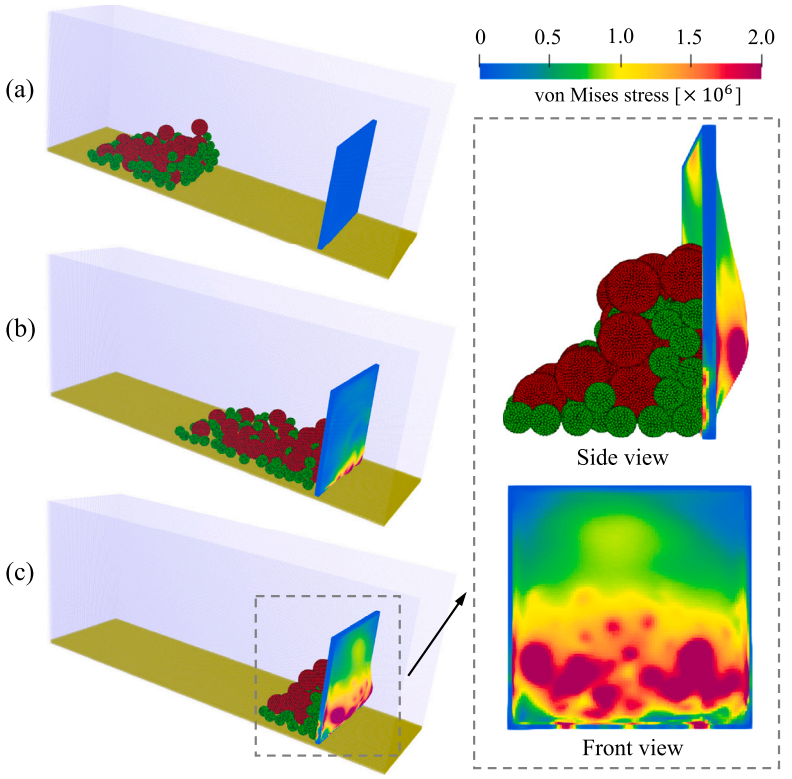

Fig. 32. Simulation process of the bouldery debris flow impacting the flexible barrier at (a) $t = 1$, (b) $t = 2$ and (c) $t = 3$. The enlarged figures on the right column depict the side view and front view of the barrier at t = 3, and the barrier is colored by von Mises stress.

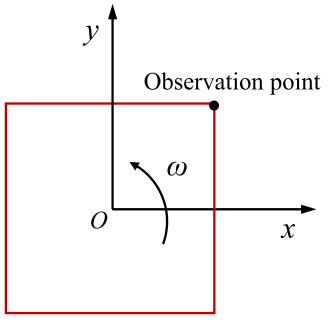

Fig. 33. Setup for the spinning plate.

Firstly, we consider the shear acceleration of particle i at time t_0 ($t_0 = 0$) based on Eq. (24)

$$\begin{aligned}\mathbf{a}_i^s(t_0) &= 2\zeta\frac{G}{\rho_i}\int_{t0}^{t1}\left(\sum_j \frac{\mathbf{e}_{ij}\cdot\mathbf{v}_{ij}}{r_{ij}}\nabla_i W_{ij}V_j\right)\mathrm{d}t \\ &= 2\zeta\frac{G}{\rho_i}\left(\sum_j \frac{\mathbf{e}_{ij}\cdot\mathbf{v}_{ij}}{r_{ij}}\nabla_i W_{ij}V_j\right)t_1\end{aligned} \tag{38}$$

The shear acceleration of particle i is influenced by a total of three particles: $\mathbf{a}_i^s(t_0) = \mathbf{a}_{i\to j_1}^s(t_0) + \mathbf{a}_{i\to j_2}^s(t_0) + \mathbf{a}_{i\to j_3}^s(t_0)$. Here, $i \to j_1$ represents the interaction between particle i and particle j_1. According to Eq. (38), the direction of $\mathbf{a}_{i\to j_1}^s(t_0)$ is along the line connecting particles i and j_1, and the same applies to interactions between other pairs of particles. Since $\mathbf{a}_{i\to j_1}^s(t_0)$ and $\mathbf{a}_{i\to j_2}^s$ have equal magnitudes, their sum is in the direction of the line connecting i and j_3, which is the direction of $\mathbf{a}_{i\to j_3}^s(t_0)$. Therefore, the direction of $\mathbf{a}_i^s(t_0)$ is along the line connecting i and j_3, as shown in the Fig. 36a. Hence, it can be calculated that at time t_0, the torque of particle i: $\tau_i(t_0) = m_i\mathbf{x}_i(t_0)\times\mathbf{a}_i^s(t_0) = 0$. Similarly, it can be computed that the torque at each of the other points is also zero. Therefore, during the transition of particle configuration from time t_0 to t_1, angular momentum of the system is conserved.

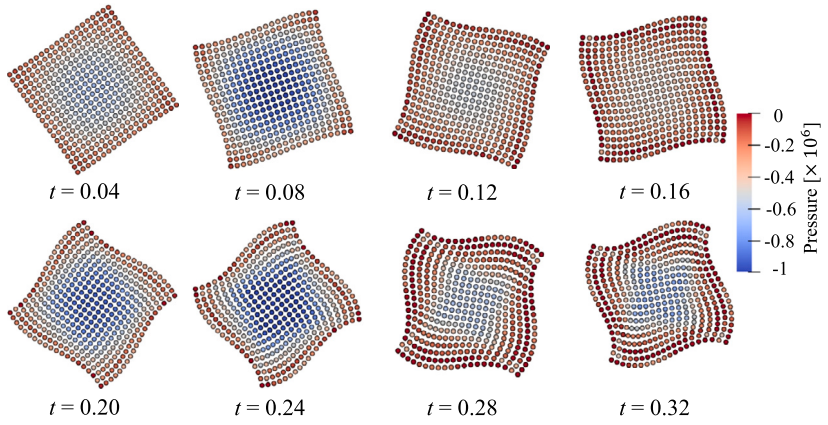

Fig. 34. The evolution of pressure and square shape at different instants for the spinning plate.

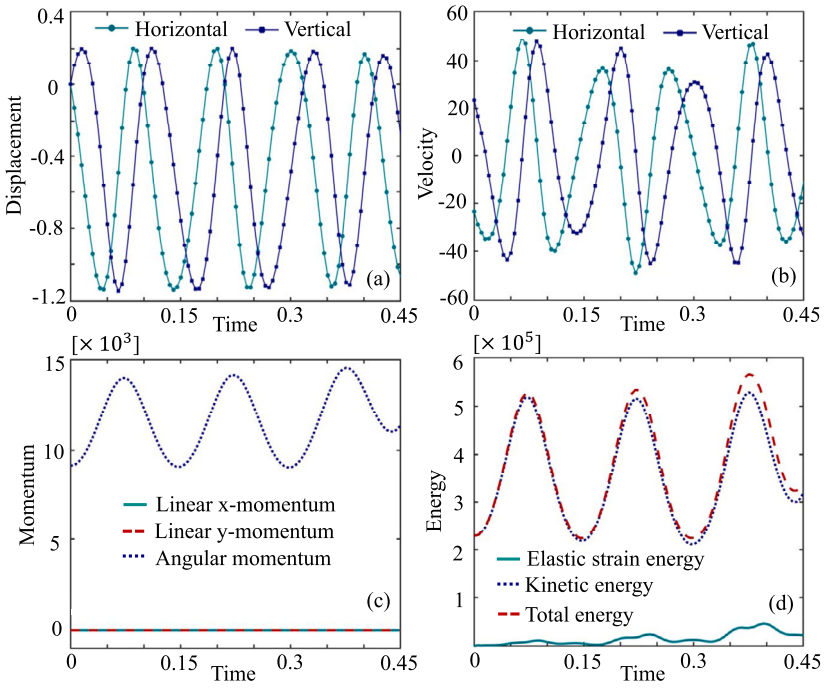

Fig. 35. The temporal evolution of some physical quantities of the spinning plate: (a) the horizontal and vertical components of displacement at the observation point; (b) the horizontal and vertical components of velocity at the observation point; (c) the total linear momentum and angular momentum of the square; (d) the elastic strain energy, kinetic energy and total energy of the square.

Subsequently, we examine the acceleration of point i at time t_1

$$\begin{aligned}\mathbf{a}_i^s(t_1) &= 2\zeta\frac{G}{\rho_i}\int_{t0}^{t2}\left(\sum_j\frac{\mathbf{e}_{ij}\cdot\mathbf{v}_{ij}}{r_{ij}}\nabla_i W_{ij}V_j\right)\mathrm{d}t\\ &= 2\zeta\frac{G}{\rho_i}\int_{t0}^{t1}\left(\sum_j\frac{\mathbf{e}_{ij}\cdot\mathbf{v}_{ij}}{r_{ij}}\nabla_i W_{ij}V_j\right)\mathrm{d}t\\ &+2\zeta\frac{G}{\rho_i}\int_{t1}^{t2}\left(\sum_j\frac{\mathbf{e}_{ij}\cdot\mathbf{v}_{ij}}{r_{ij}}\nabla_i W_{ij}V_j\right)\mathrm{d}t\\ &= \mathbf{a}_i^s(t_0)+\Delta\mathbf{a}_i^s(t_1)\end{aligned} \tag{39}$$

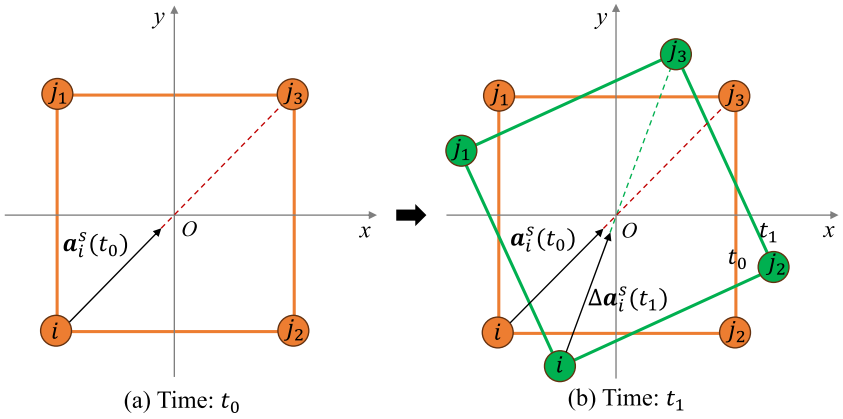

Fig. 36. Understanding the cause of angular momentum non-conservation: four particles are positioned at the four corners of a square and rotate around its center.

where $\Delta\mathbf{a}_i^s(t_1)$ represents the increment in shear acceleration calculated at time t_1. Same to the analysis for the direction of $\mathbf{a}_i^s(t_0)$, the direction of $\Delta\mathbf{a}_i^s(t_1)$ is along the line connecting i and j_3 at time t_1, as shown in the Fig. 36b. Then the torque of particle i at time t_1: $\tau_i(t_1) = m_i\mathbf{x}_i(t_1) \times \mathbf{a}_i^s(t_1) = m_i\mathbf{x}_i(t_1) \times (\mathbf{a}_i^s(t_0) + \Delta\mathbf{a}_i^s(t_1)) = m_i\mathbf{x}_i(t_1) \times \mathbf{a}_i^s(t_0)$. Due to the non-zero values of both $\mathbf{x}_i(t_1)$ and $\mathbf{a}_i^s(t_0)$, and their directions not lying on the same line, we can conclude that $\tau_i(t_1) = m_i\mathbf{x}_i(t_1) \times \mathbf{a}_i^s(t_0) \neq 0$. In addition, it can be calculated that the torques of particle j_1, j_2, and j_3, as well as particle i, are in the same direction. Therefore, the conservation of angular momentum in the system does not hold.

7. Conclusion and outlook

In this work, the numerical instability exhibited by the simulations of typical elastic dynamics problems with ULSPH is addressed in the respect of hourglass modes other than that of tensile instability. Based on such point of view, an essentially non-hourglass formulation for ULSPH by decomposing the shear acceleration with the Laplacian operator. This newly-developed method is applicable for both 2D and 3D scenarios without introducing case-dependent tuning parameters. The convergence and accuracy of the present method are verified through several fundamental test cases. The results show that the present method is numerically stable, without non-physical fractures and zigzag patterns. The stability and robustness of the non-hourglass formulation are confirmed through long-term simulations and simulations under extreme conditions. Furthermore, a dual-criteria time stepping scheme is employed to increase the calculation efficiency. For 2D and 3D oscillating plates, the computational time is reduced to approximately one-half and one-third, respectively, compared to the original calculations using single-criteria time stepping approach. It is needed to note that, the formulation does not strictly adhere to the conservation of angular momentum, which limits the application for some problems.

This research also clarified that, for the classic elastic dynamics problems, such as oscillation beam, colliding rings, etc, previously used to demonstrate tensile instability, the instability is actually due to hourglass modes other than tensile forces. This is evident by extensive numerical examples showing that after adopting a formulation handling hourglass modes, even the tensile regions are still the same, the instability vanishes. However, this clarification does not exclude tensile instabilities occur in other, especially more complex scenarios. ULSPH for solid is actually very similar to SPH for fluid except the main different model on shear stress. Since, with the standard non-hourglass formulation for fluid shear force (from which the present method is derived), the SPH fluid simulation still suffers from tensile instability, similar issues in ULSPH elastic dynamics would not be out of expectation.

It is worth mentioning that although the present formulation is proposed and validated for elastic dynamics, it is possible to extend the current work, including the point-of-view on hourglass modes and non-nested formulation, to plastic dynamics for modeling material fracture and failure. For this, we still expect to utilize the non-nested formulation to ensure numerically stability. Also note that, with more complex material model, the deformation and velocity field may be much more complex than those in elastic dynamics, one may need to further handle tensile instability.

CRediT authorship contribution statement

Shuaihao Zhang: Writing – review & editing, Writing – original draft, Visualization, Validation, Methodology, Investigation, Formal analysis, Conceptualization. **Sérgio D.N. Lourenço:** Writing – review & editing, Supervision, Investigation. **Dong Wu:** Writing – review & editing, Methodology, Investigation. **Chi Zhang:** Writing – review & editing, Methodology. **Xiangyu Hu:** Writing – review & editing, Supervision, Methodology, Investigation, Conceptualization.

Declaration of competing interest

The authors declare that they have no known competing financial interests or personal relationships that could have appeared to influence the work reported in this paper.

Data availability

The code and data are available on GitHub.

Acknowledgements

Sérgio D.N. Lourenço would like to express his gratitude to the Research Grants Council Hong Kong for their sponsorship of this research under a Collaborative Research Fund (C6006-20GF). Dong Wu, Chi Zhang and Xiangyu Hu would like to express their gratitude to the German Research Foundation (DFG) for their sponsorship of this research under grant number DFG HU1527/12-4. The computations were performed using research computing facilities offered by Information Technology Services, the University of Hong Kong.

References

[1] L.B. Lucy, A numerical approach to the testing of the fission hypothesis, Astron. J. 82 (1977) 1013–1024.
[2] R.A. Gingold, J.J. Monaghan, Smoothed particle hydrodynamics: theory and application to non-spherical stars, Mon. Not. R. Astron. Soc. 181 (3) (1977) 375–389.
[3] J.P. Morris, P.J. Fox, Y. Zhu, Modeling low Reynolds number incompressible flows using SPH, J. Comput. Phys. 136 (1) (1997) 214–226.
[4] M. Luo, C. Koh, W. Bai, M. Gao, A particle method for two-phase flows with compressible air pocket, Int. J. Numer. Methods Eng. 108 (7) (2016) 695–721.
[5] D.J. Price, Smoothed particle hydrodynamics and magnetohydrodynamics, J. Comput. Phys. 231 (3) (2012) 759–794.
[6] X.Y. Hu, N.A. Adams, A multi-phase SPH method for macroscopic and mesoscopic flows, J. Comput. Phys. 213 (2) (2006) 844–861.
[7] J.P. Gray, J.J. Monaghan, R. Swift, SPH elastic dynamics, Comput. Methods Appl. Mech. Eng. 190 (49–50) (2001) 6641–6662.
[8] G.R. Johnson, R.A. Stryk, S.R. Beissel, SPH for high velocity impact computations, Comput. Methods Appl. Mech. Eng. 139 (1–4) (1996) 347–373.
[9] C.H. Lee, A.J. Gil, A. Ghavamian, J. Bonet, A total Lagrangian upwind smooth particle hydrodynamics algorithm for large strain explicit solid dynamics, Comput. Methods Appl. Mech. Eng. 344 (2019) 209–250.
[10] C.H. Lee, A.J. Gil, J. Bonet, Development of a cell centred upwind finite volume algorithm for a new conservation law formulation in structural dynamics, Comput. Struct. 118 (2013) 13–38.
[11] C.H. Lee, P.R. Refachinho de Campos, A.J. Gil, M. Giacomini, J. Bonet, An entropy-stable updated reference Lagrangian smoothed particle hydrodynamics algorithm for thermo-elasticity and thermo-visco-plasticity, Computational Particle Mechanics 10 (6) (2023) 1493–1531.
[12] C. Antoci, M. Gallati, S. Sibilla, Numerical simulation of fluid–structure interaction by SPH, Comput. Struct. 85 (11–14) (2007) 879–890.
[13] A. Khayyer, H. Gotoh, Y. Shimizu, Y. Nishijima, A 3D Lagrangian meshfree projection-based solver for hydroelastic fluid-structure interactions, J. Fluids Struct. 105 (2021) 103342.
[14] A. Khayyer, H. Gotoh, H. Falahaty, Y. Shimizu, An enhanced isph–sph coupled method for simulation of incompressible fluid–elastic structure interactions, Comput. Phys. Commun. 232 (2018) 139–164.
[15] S.-C. Hwang, A. Khayyer, H. Gotoh, J.-C. Park, Development of a fully Lagrangian mps-based coupled method for simulation of fluid–structure interaction problems, J. Fluids Struct. 50 (2014) 497–511.
[16] R. Vignjevic, J.R. Reveles, J. Campbell, SPH in a total Lagrangian formalism, CMC 4 (3) (2006) 181.
[17] J.J. Monaghan, SPH without a tensile instability, J. Comput. Phys. 159 (2) (2000) 290–311.
[18] J.W. Swegle, D.L. Hicks, S.W. Attaway, Smoothed particle hydrodynamics stability analysis, J. Comput. Phys. 116 (1) (1995) 123–134.
[19] P. Randles, L.D. Libersky, Smoothed particle hydrodynamics: some recent improvements and applications, Comput. Methods Appl. Mech. Eng. 139 (1–4) (1996) 375–408.
[20] G.R. Johnson, S.R. Beissel, Normalized smoothing functions for SPH impact computations, Int. J. Numer. Methods Eng. 39 (16) (1996) 2725–2741.
[21] C. Dyka, P. Randles, R. Ingel, Stress points for tension instability in SPH, Int. J. Numer. Methods Eng. 40 (13) (1997) 2325–2341.
[22] J. Bonet, S. Kulasegaram, Remarks on tension instability of Eulerian and Lagrangian corrected smooth particle hydrodynamics (CSPH) methods, Int. J. Numer. Methods Eng. 52 (11) (2001) 1203–1220.
[23] T. Belytschko, S. Xiao, Stability analysis of particle methods with corrected derivatives, Comput. Math. Appl. 43 (3–5) (2002) 329–350.
[24] D. Mandell, C. Wingate, L. Schwalbe, Computational brittle fracture using smooth particle hydrodynamics, Tech. Rep., Los Alamos National Lab. (LANL), Los Alamos, NM (United States), 1996.
[25] G.A. Dilts, Moving-least-squares-particle hydrodynamics—I. Consistency and stability, Int. J. Numer. Methods Eng. 44 (8) (1999) 1115–1155.
[26] P. Randles, L. Libersky, Normalized SPH with stress points, Int. J. Numer. Methods Eng. 48 (10) (2000) 1445–1462.
[27] C. Zhang, X.Y. Hu, N.A. Adams, A generalized transport-velocity formulation for smoothed particle hydrodynamics, J. Comput. Phys. 337 (2017) 216–232.
[28] L. Lobovskỳ, J. Křen, Smoothed particle hydrodynamics modelling of fluids and solids, 2007.
[29] C. Peng, S. Wang, W. Wu, H.S. Yu, C. Wang, J.Y. Chen, LOQUAT: an open-source GPU-accelerated SPH solver for geotechnical modeling, Acta Geotech. 14 (2019) 1269–1287.
[30] H.H. Bui, G.D. Nguyen, Smoothed particle hydrodynamics (SPH) and its applications in geomechanics: from solid fracture to granular behaviour and multiphase flows in porous media, Comput. Geotech. 138 (2021) 104315.
[31] A. Khayyer, Y. Shimizu, C.H. Lee, A. Gil, H. Gotoh, J. Bonet, An improved updated Lagrangian SPH method for structural modelling, Computational Particle Mechanics (2023) 1–32.
[32] G.C. Ganzenmüller, An hourglass control algorithm for Lagrangian smooth particle hydrodynamics, Comput. Methods Appl. Mech. Eng. 286 (2015) 87–106.
[33] D. Wu, C. Zhang, X. Tang, X. Hu, An essentially non-hourglass formulation for total Lagrangian smoothed particle hydrodynamics, Comput. Methods Appl. Mech. Eng. 407 (2023) 115915.
[34] C. Zhang, M. Rezavand, X. Hu, Dual-criteria time stepping for weakly compressible smoothed particle hydrodynamics, J. Comput. Phys. 404 (2020) 109135.
[35] C. Zhang, M. Rezavand, Y. Zhu, Y. Yu, D. Wu, W. Zhang, J. Wang, X. Hu, SPHinXsys: an open-source multi-physics and multi-resolution library based on smoothed particle hydrodynamics, Comput. Phys. Commun. 267 (2021) 108066.
[36] C. Zhang, X. Hu, N.A. Adams, A weakly compressible SPH method based on a low-dissipation Riemann solver, J. Comput. Phys. 335 (2017) 605–620.
[37] S. Zhang, C. Zhang, X. Hu, S.D. Lourenço, A Riemann-based SPH method for modelling large deformation of granular materials, Comput. Geotech. 167 (2024) 106052.
[38] P. Espanol, M. Revenga, Smoothed dissipative particle dynamics, Phys. Rev. E 67 (2) (2003) 026705.
[39] X. Hu, N. Adams, Angular-momentum conservative smoothed particle dynamics for incompressible viscous flows, Phys. Fluids 18 (10) (2006).
[40] R. Vignjevic, J. Campbell, L. Libersky, A treatment of zero-energy modes in the smoothed particle hydrodynamics method, Comput. Methods Appl. Mech. Eng. 184 (1) (2000) 67–85.
[41] R. Vignjevic, J. Campbell, Review of development of the smooth particle hydrodynamics (SPH) method, in: Predictive Modeling of Dynamic Processes: A Tribute to Professor Klaus Thoma, Springer, 2009, pp. 367–396.

[42] J. Swegle, S. Attaway, M. Heinstein, F. Mello, D. Hicks, An analysis of smoothed particle hydrodynamics, Sandia report no, Tech. Rep., SAND93-2513-UC-705, 1994.
[43] J.J. Monaghan, Smoothed particle hydrodynamics, Rep. Prog. Phys. 68 (2005) 1703–1759.
[44] J.J. Monaghan, R.A. Gingold, Shock simulation by the particle method sph, J. Comput. Phys. 52 (2) (1983) 374–389.
[45] P.W. Cleary, Modelling confined multi-material heat and mass flows using sph, Appl. Math. Model. 22 (12) (1998) 981–993.
[46] P. Cleary, J. Ha, V. Alguine, T. Nguyen, Flow modelling in casting processes, Appl. Math. Model. 26 (2) (2002) 171–190.
[47] A. Colagrossi, M. Antuono, A. Souto-Iglesias, D. Le Touzé, Theoretical analysis and numerical verification of the consistency of viscous smoothed-particle-hydrodynamics formulations in simulating free-surface flows, Phys. Rev. E 84 (2) (2011) 026705.
[48] S.J. Cummins, M. Rudman, An sph projection method, J. Comput. Phys. 152 (2) (1999) 584–607.
[49] C. Zhang, M. Rezavand, X. Hu, A multi-resolution SPH method for fluid-structure interactions, J. Comput. Phys. 429 (2021) 110028.
[50] H. Wendland, Piecewise polynomial, positive definite and compactly supported radial functions of minimal degree, Adv. Comput. Math. 4 (1995) 389–396.
[51] J. Bonet, S. Kulasegaram, A simplified approach to enhance the performance of smooth particle hydrodynamics methods, Appl. Math. Comput. 126 (2–3) (2002) 133–155.
[52] C. Zhang, J. Wang, M. Rezavand, D. Wu, X. Hu, An integrative smoothed particle hydrodynamics method for modeling cardiac function, Comput. Methods Appl. Mech. Eng. 381 (2021) 113847.
[53] L.D. Landau, E.M. Lifshitz, Course of Theoretical Physics, Elsevier, 2013.
[54] A.W. Leissa, Vibration of Plates, Scientific and Technical Information Division, vol. 160, National Aeronautics and Space Administration, 1969.
[55] Y. Yu, Y. Zhu, C. Zhang, O.J. Haidn, X. Hu, Level-set based pre-processing techniques for particle methods, Comput. Phys. Commun. 289 (2023) 108744.
[56] L. Bugnion, B.W. McArdell, P. Bartelt, C. Wendeler, Measurements of hillslope debris flow impact pressure on obstacles, Landslides 9 (2012) 179–187.
[57] D. Song, C.E. Choi, C.W.W. Ng, G.G. Zhou, J.S. Kwan, H. Sze, Y. Zheng, Load-attenuation mechanisms of flexible barrier subjected to bouldery debris flow impact, Landslides 16 (2019) 2321–2334.
[58] C. Johnson, B. Kokelaar, R.M. Iverson, M. Logan, R. LaHusen, J. Gray, Grain-size segregation and levee formation in geophysical mass flows, J. Geophys. Res., Earth Surf. 117 (F1) (2012).